SUPERCONDUCTING QUANTUM INTERFERENCE DEVICE ARRAY BASED HIGH FREQUENCY DIRECTION FINDING ON AN AIRBORNE PLATFORM

THESIS

Tyrel K. Kvasager, Capt, USAF

AFIT-ENG-MS-16-M-028

DEPARTMENT OF THE AIR FORCE
AIR UNIVERSITY

AIR FORCE INSTITUTE OF TECHNOLOGY

Wright-Patterson Air Force Base, Ohio

AFIT-ENG-MS-16-M-028

SUPERCONDUCTING QUANTUM INTERFERENCE DEVICE ARRAY BASED HIGH FREQUENCY DIRECTION FINDING ON AN AIRBORNE PLATFORM

THESIS

Presented to the Faculty

Department of Electrical and Computer Engineering

Graduate School of Engineering and Management

Air Force Institute of Technology

Air University

Air Education and Training Command

in Partial Fulfillment of the Requirements for the

Degree of Master of Science in Electrical Engineering

Tyrel K. Kvasager, B.S.E.E.

Capt, USAF

March 2016

AFIT-ENG-MS-16-M-028

SUPERCONDUCTING QUANTUM INTERFERENCE DEVICE ARRAY BASED HIGH FREQUENCY DIRECTION FINDING ON AN AIRBORNE PLATFORM

THESIS

Tyrel K. Kvasager, B.S.E.E.
Capt, USAF

Committee Membership:

LtCol J. Stringer, PhD
Chair

Maj M. Seal, PhD
Member

Maj S. Stone, PhD
Member

Abstract

This thesis evaluates a new incredibly sensitive highly linear high dynamic range 2D Bi-Superconducting Quantum Interference Device (Bi-SQUID) array purposed by the dissertation written by Susan Berggren [1] applied to use on an airborne platform for the purposes of High Frequency Direction Finding (HFDF). To evaluate how useful the 2D Bi-SQUID is we explore multiple signals of the same frequency in two different base sensor configurations: Non-uniform phased array and non-colocated Poynting's Theorem based vector sensors. The exploration is performed using a series of simulations using the Spirit High Performance Computing Modernization Program (HPCMP) system to calculate the 2D Bi-SQUID output given multiple incident signals. The Angle of Arrival (AoA) estimation calculation is performed using the Multi-Signal Classification (MUSIC) algorithm on the signals received on the non-uniform phased array, and the Estimation of Signal Parameters via Rotational Invariance Techniques (ESPRIT) algorithm is used on the signals received on the non-colocated vector sensor. The simulation results show that the MUSIC algorithm using 2D Bi-SQUIDs is able to differentiate two signals that are of the same frequency, but the resolution and accuracy of the algorithm is poor due to the size of the phased array on the airborne platform. The non-colocated ESPRIT using 2D Bi-SQUIDs performs better, but still has less than desirable angular error. The research determined that with the 2D Bi-SQUID technology, the ability to receive the signal need not be the catching point for electrically small Direction Finding (DF) algorithms to achieve the desired level of accuracy.

AFIT-ENG-MS-16-M-028

To my beautiful loving wife and

my two wonderful rambunctious sons

Acknowledgements

First I would like to thank my thesis advisor, Lt Col Jeremy Stringer, PhD whose guidance made this all possible. I would also like to thank my committee members, Major Micheal Seal, PhD and Major Samuel Stone, PhD for taking the time to review this work. Finally I would like to thank Dr. Susan Berggren at Space and Naval Warfare Systems Command (SPAWAR) for providing much needed assistance in understanding her complex model used as the backbone for the 2D Bi-SQUID simulation in this thesis.

Tyrel K. Kvasager

Table of Contents

Page

List of Figures

List of Tables

SUPERCONDUCTING QUANTUM INTERFERENCE DEVICE ARRAY BASED HIGH FREQUENCY DIRECTION FINDING ON AN AIRBORNE PLATFORM

I. Problem Statement

The High Frequency (HF) band is the portion of the electromagnetic (EM) spectrum with a frequency between 3 and 30 MHz with a wavelength of 100 to 10 meters respectively. Where frequency is the number of times in a second the signal oscillates, and the wavelength is the distance between two peaks in an oscillation. The HF band is used for amateur radio operation, long range inter-continental communication, international shortwave broadcasting, and distress signals.

High Frequency Direction Finding (HFDF) is the process of determining the direction a signal originated from using an antenna array paired with receiver hardware and a software algorithm. The problem with either of these methods, when looking at an HF signal, is that the system needs to be able to determine the phase of the signal to estimate the direction of arrival. An array size of more then one wavelength is desirable for optimal Angle of Arrival (AoA) estimation. An array of 1.5 wavelengths is 150 meters (492 feet) long for the longest wavelength in the HF spectrum. Unfortunately, the largest aircraft in the United States arsenal is the C-5 Galaxy which has a wingspan of about 222 feet and is 247 feet long, which is still too small for a desirable array size. HFDF is vital to search and rescue, Signals Intelligence (SIGINT) and other Intelligence, Surveillance and Reconnaissance (ISR) functions. The ability to perform HFDF function on an airborne platform is exceedingly more valuable because of the agility an airborne platform provides. Thus, research in electrically

small antennas and arrays continues.

1.1 Purpose

The line of research pursued in this thesis has been explored within the Air Force Institute of Technology (AFIT) and other notable institutions by a series of students, and is sponsored by the Air Force Research Laboratory (AFRL) as well as the Space and Naval Warfare Systems Command (SPAWAR). AFRL and SPAWAR recognize the advantage of adding the HF band into usable spectrum for both ships and aircraft. The fundamental goal of each piece of research has been to install a HFDF array on a RC-135 airframe. There has been varying success in this area, most of which has been eliminating possible solutions due to inadequate performance. This extension onto the line of possible solutions is to investigate the viability of Superconducting Quantum Interference Device (SQUID) sensors as an alternative to traditional electrically small antennas and amplifier hardware solutions.

1.2 Background

Early research in HFDF was focused on structurally integrated antennas in various configurations. Some were as simple as a long cable running from mid-fuselage to the tail of an RC-135 [4] as seen in Figure 1. Another research path was to strategically place structurally integrated antennas on an RC-135 [4]. The most recent research branch departed from the use of antennas which measure the electric $\overrightarrow{E}$ field and turned instead to measuring the magnetic $\overrightarrow{H}$ field using the relationship $\overrightarrow{E} = \eta\overrightarrow{H}$. The $\overrightarrow{H}$ field sensor explored was the MGL-S8A B-dot sensor. The B-dot sensor was determined to not be suitable of HFDF due to a insufficient sensitivity. After the B-dot sensor was investigated, the author suggested examining SQUID arrays [3].

SQUIDs are highly sensitive devices that convert magnetic flux or fields into a

Figure 1. Variant of RC-135 with a cable antenna attached at mid-fuselage to mid-tail. (U.S. Air Force photo/Tech. Sgt. Deborah Davis)

voltage that can be sampled to digitally process the signal. All radio waves are self sustaining electromagnetic waves consisting of an electric component and an orthogonal magnetic portion. SQUIDs are ultra sensitive devices which can detect incredibly small magnetic field levels. This sensitivity can also be detrimental as shown in [5] where small signals cause the Direct Current Superconducting Quantum Interference Device (DC-SQUID) to saturate, meaning that the output of the device did not correspond linearly to the input. In a standard amplifier, saturation is observed when looking at a sinusoidal signal which has had it peak clipped off flat. The region prior to saturation is referred to as the linear region. Bi-Superconducting Quantum Interference Devices (Bi-SQUIDs) have been shown to have a larger linear range then the standard DC-SQUID [1, 2].

2D Bi-SQUIDs are SQUID arrays with Bi-SQUIDs in both serial and parallel configuration. The 2D configuration was found to have a larger range of linearity when arranged in arrays, and a dynamic range more suitable to signal reconstruction then the saturation sensitive single DC-SQUID or Bi-SQUID [1].

1.3 The Problem

Installing an antenna array that is suitable to receive HF signals and estimate the AoA is difficult to accomplish because the wavelength of an HF signal ranges from 10 to 100 meters long. The wavelength determines the electrical size of an antenna. If an antenna is larger than the wavelength of the signal, then the antenna is considered electrically large. If an antenna is smaller than the wavelength of the signal it is considered electrically small. Electrically small antennas have a prohibitively poor radiation pattern, which results in poor performance when signal strengths are low.

SQUIDs are highly sensitive devices that are capable of detecting as low as a few flux quantum of magnetic flux (less then the magnetic field associated with brain waves), but tend to be non-linear; thus making it difficult to extract phase data from the sensor. The ultra sensitivity also results in a low dynamic-range. Dynamic-range is the amount of power variation the received signal can demonstrate and still be accurately observed. Bi-SQUIDs use a third Josephson junction to improve the linearity [6]. The 2D Bi-SQUID arrays further improve linearity and dynamic range by making the SQUID loop area a Gaussian distributed random size [1]. This output provides a larger linear range when compared to the normal DC-SQUID.

Past works have used SQUID elements in electrically large arrays, and co-located vector sensor cubes. The purpose of this research is to investigate the applicability of SQUID technology to HFDF of multiple co-band signals some sharing the same transmit frequency using an electrically small array and non-colocated vector sensor.

1.4 Assumptions and Limitations

The scope of this research effort is confined to:

1. The HF band, consisting of the frequencies 3 MHz to 30 MHz.

2. The radiation pattern for each antenna element is considered isotropic.

3. The propagation media is homogeneous and lossless for the EM wave.

4. The EM wave propagation is in unbounded free space.

5. All multi-path effects are neglected.

6. All signal sources are considered to be in the far-field, resulting in a plane wave traveling across the antenna array.

7. The distribution of magnetic flux is uniform across the SQUID sensor.

8. The location of each sensor in the array is perfectly known.

9. Electric field vector sensor dipole elements are considered ideal (0 dBi Gain) with no noise and perfect field sensing.

1.5 Methodology and Resources

This research is achieved by using the Bi-SQUID model developed by Susan Berggren at SPAWAR in her dissertation [1], modified to improve efficiency and adapted to compile on the Spirit High Performance Computing (HPC) system. The model is fed either tone signals or gold code signals, and processes at the location of each sensor across the RC-135. The signal travel time is simulated using a phase shift term for the tone signals, and a time based circular shift for the gold coded signals. Two methods of direction finding are explored: Nonlinear array Multi-Signal Classification (MUSIC) algorithm and vector sensor Estimation of Signal Parameters via Rotational Invariance Techniques (ESPRIT) algorithm. The vector sensor approach requires three orthogonal Bi-SQUID sensors per point in the array and three orthogonal dipole antennas. The Nonlinear array method requires only one Bi-SQUID sensor per point in the array.

This research is achieved by using a model of the individual Bi-SQUID array. Each Bi-SQUID array is considered a single sensor. The MATLAB® simulation scenarios consist of various sensor array configurations (arrays of Bi-SQUID arrays). Each simulation scenario will be evaluated for signal strength, dynamic range, and the ability to recover the phase information from the signal.

1. The simulations will be performed in the Matrix Laboratory version 2015a.

2. The signals are constructed on a computer workstation containing Intel Xeon processor with 8 logical cores and 32 GB of RAM.

3. The Bi-SQUID sensor simulations are computed on the High Performance Computing Modernization Program (HPCMP) Spirit cluster.

4. Each data run requires approximately 50 minutes to run for each sensor simulated on SPIRIT.

1.6 Overview

This thesis presents an analysis of the 2D Bi-SQUID array sensor modeled by Susan Berggren with an alternate application of radar and HFDF tasks. The analysis consists of an evaluation of the performance of 2D Bi-SQUID sensors in an undersized non-uniform phased array and on the non-colocated vector sensor array configurations' ability to distinguish co-channel signals, and resolve the AoA of the signals. Chapter 2 reviews recent research in the area of SQUID technology and modeling techniques. Chapter 3 discusses the methods used to estimate the AoA for the HF signals, a verification of each implementation, and finally the experiment setup. Chapter 4 presents the data collected and analyzes the suitability of the Bi-SQUID sensors and Direction Finding (DF) algorithms for the HFDF application. Chapter 5

discusses the viability of using the Bi-SQUID design for an electrically small HFDF antenna, and a recommendation for further research in the area of HFDF sensors.

II. Literature Review

The literature review focuses on the research already conducted on the chosen High Frequency Direction Finding (HFDF) sensor, the Superconducting Quantum Interference Device (SQUID). We will start with superconductivity and the properties of a superconductor. We will look at SQUIDs of various configurations; concluding the study with a review of what is known of our chosen 2D Bi-Superconducting Quantum Interference Device (Bi-SQUID) sensor.

2.1 Superconductivity

Superconductivity was discovered in 1911 by Dutch physicist Heike K. Onnes. The first superconducting metal was mercury. Mercury was found to have reached the superconducting state at the critical temperature $T_c \simeq 4.2K$, below which it exhibited nearly zero resistance, as seen in a plot from his labbook in Figure 2 [7].

2.1.1 Properties.

The charge carriers of a metal that is not a superconductor or a superconducting metal that is not below its critical temperature (T_c) can be excited and scattered independently. Below T_c, the superconductor charge carriers become strongly correlated. These correlated charge carriers form pairs called Cooper pairs. A Cooper pair consists of holes or electrons. Cooper pairs allow the use of the macroscopic wave function (2-1) where Ψ_0^2 is proportional to the density of the Cooper pairs, and the phase term φ describes the motion of the Cooper pairs around the superconducting loop [8].

$$\Psi\left(\overrightarrow{r}, t\right) = \Psi_0\left(\overrightarrow{r}, t\right) \exp\left[i\varphi\left(\overrightarrow{r}, t\right)\right] \tag{2-1}$$

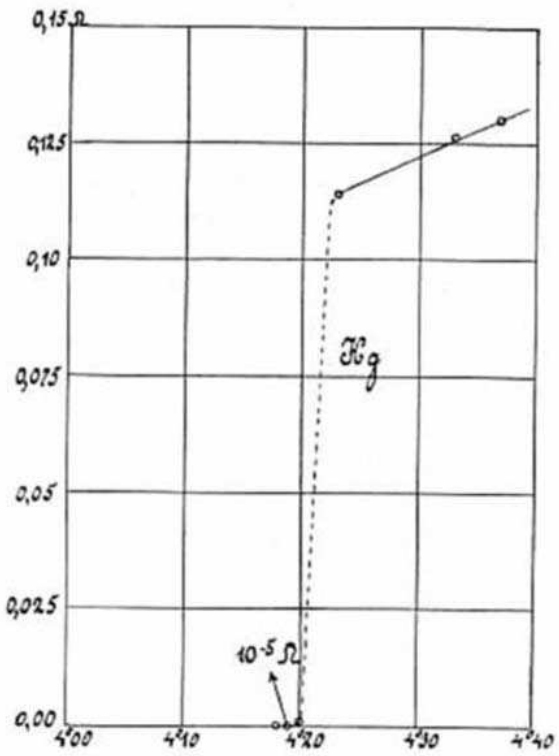

Figure 2. Resistance plot from Onnes' notebook 56, dated 26 October 1911 [7].

One of the key properties of a superconductor is that the Cooper pairs possesses a well-defined phase when formed in a superconducting loop. In the absence of magnetic flux threading the superconducting loop, $\varphi\left(\overrightarrow{r}, t\right)$ in (2-1) take the same phase value for all Cooper pairs. When magnetic flux threads the superconducting loop, the phase changes by $2\pi n$ around the loop, where n is the number of flux quanta threading, Φ_0, the loop [8].

There are two types of superconductors, low-temperature (type 1) and high-temperature (type 2). The low-temperature superconductors consist of simple metals like mercury, lead and niobium, which have a $T_c < 30K$. The high-temperature superconducting materials consist of complex alloys like bismuth-strontium-calcium-copper-oxide (BSCCO), thallium-barium-calcium-copper-oxide (TBCCO), and yttrium-barium-copper-oxide (YBCO). The high-temperature superconductors have a $T_c > 30K$, and some can achieve superconductivity at temperatures as high as $150K$ under

high pressure [9].

2.2 Josephson Junctions

Josephson junctions consist of two weakly coupled superconducting electrodes separated by either a normal metal, as in the SNS type junction, or an insulator, as in the SIS type junction [8]. A new fabrication technique that has been recently demonstrated to be stable, uses high-critical temperature (T_c) superconducting materials, like YBCO, and illuminates a narrow strip by using ion irradiation. Ion irradiation lowers the T_c and increases the resistivity of the YBCO material illuminated. The nano-channel created by the illumination acts like a normal metal creating a SNS type junction [10].

If the junction is properly constructed, the supercurrent I_s across the junction is functionally dependent to the gauge invariant phase difference seen in (2-2) as δ and the critical current I_0. The φ terms are the phase of the superconducting condensates of the 2 electrodes.

$$\delta = \varphi_1 - \varphi_2 \tag{2-2}$$

The critical current is the input bias current required for the SQUID to operate in resistive mode making the output voltage of the SQUID a function of input magnetic flux. Equation (2-3) is considered the first Josephson equation [8].

$$I_s = I_0 \sin \delta \tag{2-3}$$

The second Josephson equation (2-4) relates the change in gauge invariant phase difference with respect to time $\frac{d\delta}{dt}$ to the voltage U developed across the junction. The voltage forms from the phase difference in accordance with (2-4) once $I_s \geq I_0$ [8].

$$\dot{\delta} \equiv \frac{d\delta}{dt} = \frac{2e}{\hbar}U = \frac{2\pi}{\Phi_0}U \tag{2-4}$$

Where

$$\begin{aligned} \Phi_0 &= \frac{h}{2e} \simeq 2.07 \times 10^{-15}\,(V \cdot s) && (2\text{-}5)\\ h &= 2\pi\hbar\,(eV \cdot s) && (2\text{-}6)\\ \hbar &= \text{Planck's Constant}\,(eV \cdot s)\\ e &= \text{charge of an electron}\,(C) \end{aligned}$$

SQUIDs have been configured in a variety of ways to achieve desirable characteristics for a plethora of purposes.

2.3 Superconducting Quantum Interference Devices

There are three primary SQUID configurations in common use, the Direct Current Superconducting Quantum Interference Device (DC-SQUID), Radio Frequency Superconducting Quantum Interference Device (RF-SQUID), and the Bi-SQUID. Each of these configuration uses Josephson junctions to achieve their desired purpose.

2.3.1 DC-SQUID.

The DC-SQUID is the most sensitive of the SQUIDs created to date. This device contains two Josephson junctions, each with a shunt resister to reduce hysteresis around the loop. The schematic in Figure 3 also shows a capacitor in the model [8]. This capacitor represents the self-capacitance in the Josephson junction.

Captain Abeita explored the DC-SQUID in his thesis [5]. The simulation configuration he chose for his research use a single DC-SQUID and modeled the output of a

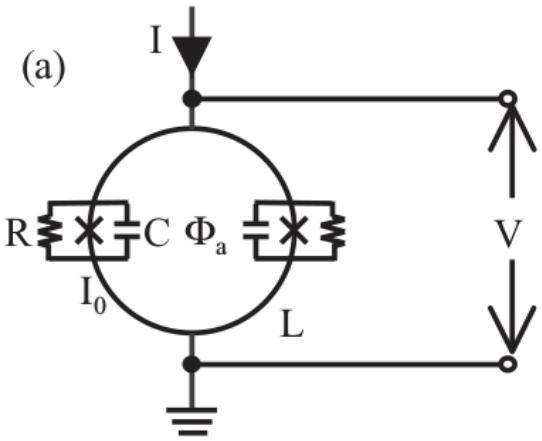

Figure 3. DC-SQUID Schematic

single device. He found that the sensitivity of the device was high, but the dynamic range of was not great enough to perform the Direction Finding (DF) calculations on a High Frequency (HF) signal [5]. This configuration is not effective.

Fortunately, SQUIDs have higher gain, better dynamic range, and linearity performance when in arrays [11, 12, 13]. The use of single SQUID designs would result in a wide variation in device performance due to geometric inconsistencies that occur during fabrication. The inconsistencies would result in significant waste or a significant calibration cost. The geometry of the SQUIDs governs amount of flux (Φ) threading an area in accordance with (2-7), where B is the magnetic flux density, w is the width of the non-superconducting barrier, d is the barrier thickness and λ is the London penetration depth of the 2 superconductors [8, p. 3-4]. The London penetration depth is a material parameter found in [8, p. 361].

$$\Phi = Bw\,(d + \lambda_1 + \lambda_2) \tag{2-7}$$

The effects of geometric inconsistencies are mitigated by array configurations [1].

2.3.2 RF-SQUID.

An RF-SQUID consists of a superconducting loop with a single Josephson junction. Therefore the RF-SQUID is not actually a SQUID because it lacks the interference-causing second Josephson junction [8]. Instead, it is a loop that is inductively coupled with an Radio Frequency (RF) tank circuit. The tank circuit has a coupling coil which is damped to prevent hysteresis using shunt resistive and capacitive components, which feed into an amplifier as seen in Figure 4 [8, p. 13].

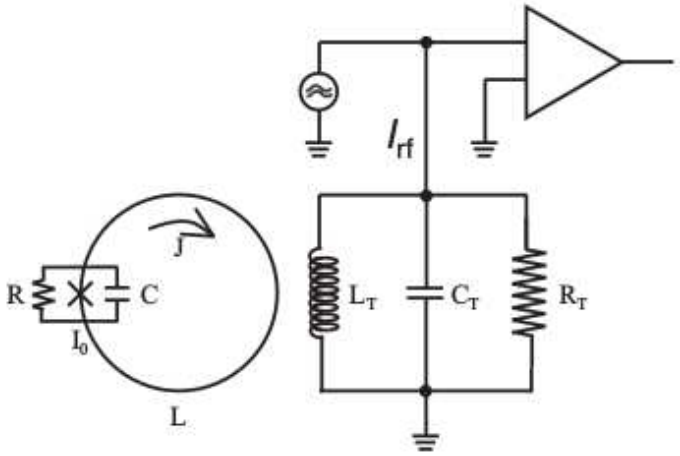

Figure 4. RF-SQUID Schematic [8]

RF-SQUIDs have a higher thermal noise component due to the additional of an amplifier at room temperature. RF-SQUIDs also have a higher $1/f$ flux noise than DC-SQUIDs [8, p. 16]. The high thermal noise associated with the RF-SQUID eliminates one of the key advantages of using SQUIDs, removing it as a viable configuration this work.

2.3.3 Bi-SQUID.

The Bi-SQUID, also referred to as a Superconducting Quantum Interference Filter (SQIF), has a third Josephson junction dividing the main SQUID as seen in Figure 5 [2]. The third junction improves the linearity of the device by modifying the nonlinear

transfer function of a DC-SQUID, producing an average voltage response with higher linearity. The non-linearity of the junctions combine to produce a linear output[2, 6, 14].

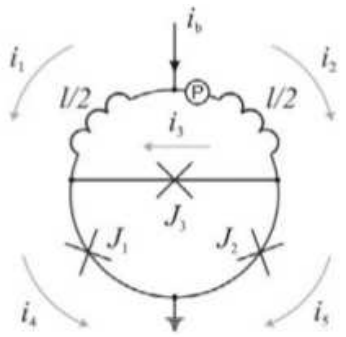

Figure 5. Bi-SQUID Circuit Diagram [2].

Bi-SQUIDs can be configured in arrays to further refine the output characteristics and optimize the performance toward a specified goal.

2.3.4 SQUID Arrays.

When **SQUUID!**s (**SQUUID!**s) are configured in arrays dynamic range improves for both series and parallel arrays by a factor of $\sqrt{N}$ where N is the number of SQUIDs in the array, and ouput voltage noise decreases by the same factor of $\sqrt{N}$ [2].

The initial building block for the graphical representation of the 2D Bi-SQUID array is seen in Figure 6. In Figure 6 the currents are shown as $(i_1, i_2, i_3, i_4, i_5, i_6, i_7, i_b)$ where each of the numbered currents describe the current through a branch of the device and i_b describes the bias current. The labels φ_1, φ_2 and φ_3 describe the condensate phase through the Josephson junctions, and $(L_{1a}, L_{1b}, L_{2a}, L_{2b}, L_{3a}, L_{3b})$ describe the inductance in each branch. The $\times$ is the location of the Josephson junction [1].

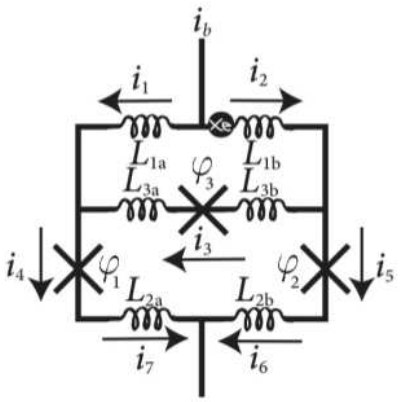

Figure 6. Bi-SQUID Circuit Diagram [1].

The currents are given by

$$\begin{aligned} i_b &= i_1 + i_2 \\ i_4 &= i_1 + i_3 \\ i_2 &= i_3 + i_5 \\ i_4 &= \sin\varphi_1 + \dot{\varphi}_1 \\ i_5 &= \sin\varphi_2 + \dot{\varphi}_2 \\ i_3 &= i_{c3}\sin\varphi_3 + \dot{\varphi}_3, \end{aligned} \tag{2-8}$$

where i_{c3} is the normalized critical current of third junction [1].

When connected in serial, the Bi-SQUIDs are connected at the end nodes as seen in Figure 7. When connected in parallel the adjacent Bi-SQUIDs share a Josephson junction as seen in Figure 8.

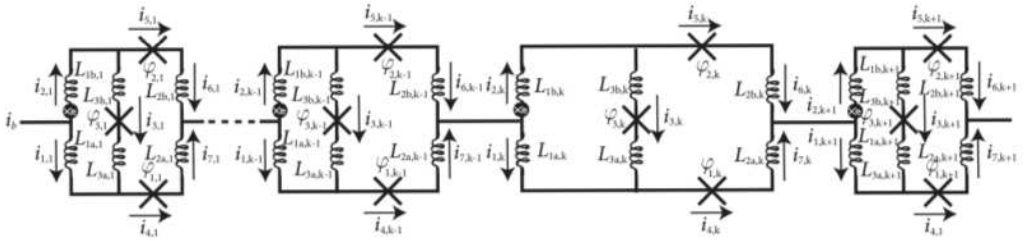

Figure 7. Serial Bi-SQUID Array Circuit Diagram [1].

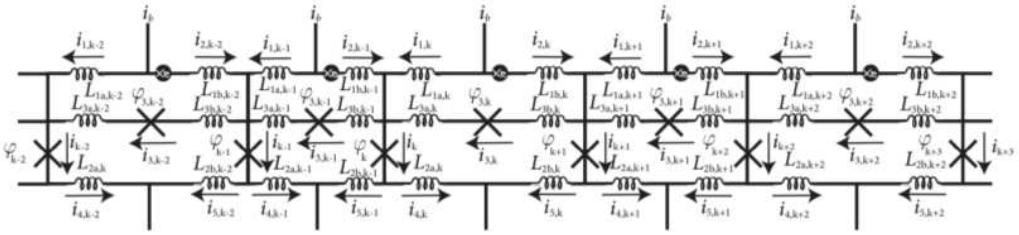

Figure 8. Parallel Bi-SQUID Array Circuit Diagram [1].

This thesis uses 2D Bi-SQUID sensors, meaning that the sensors contain both parallel and serial arrays which connect as seen in Figure 9. The 2D configuration is used because it was found experimentally to be linear and have suitable dynamic range to function as a signal receiver by Dr. Berggren, and selected for prototype fabrication.

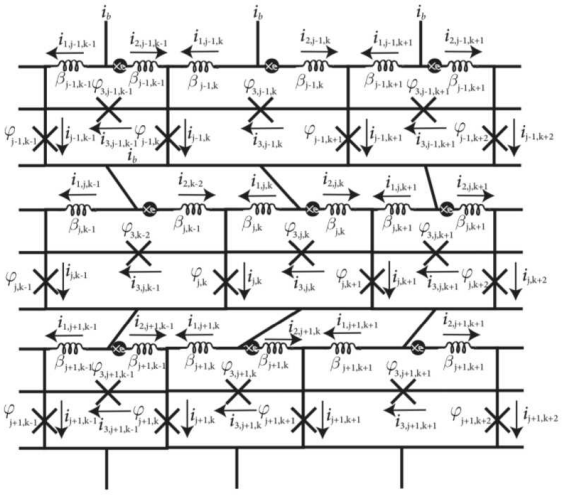

Figure 9. 2D Bi-SQUID Array Circuit Diagram [1].

2.4 2D Bi-SQUID Model

This SQUID model uses a 2D Bi-SQUID array with 85 Bi-SQUIDs in series and 12 of the series chains in parallel. The Bi-SQUID loop areas are pulled at random from a Gaussian distribution, $\mathcal{N}(0, D/\tau)$, where $D = 10^{-6}$. The inter-SQUID coupling strength β is set to 0.01.

The equations governing the dynamics of the 2D model are generated using Kirchhoff's current law to generate the phase relationships across the Josephson's junctions. For a full explanation please see [1]. The interior dynamics are given by

$$
\begin{aligned}
2\dot{\varphi}_{1,1} - \dot{\varphi}_{1,2} &= \frac{i_b}{2} + \frac{1}{\beta_{1,1}}\left(\varphi_{e,1,1} + \varphi_{1,2} - \varphi_{1,1}\right) - \sin\left(\varphi_{1,1}\right) \\
&\quad + i_{c_3,1,1}\sin\left(\varphi_{1,2} - \varphi_{1,1}\right) \\
-\dot{\varphi}_{1,k-1} + 3\dot{\varphi}_{1,k} - \dot{\varphi}_{1,k+1} &= i_b + \frac{1}{\beta_{1,k}}\left(\varphi_{e,1,k} + \varphi_{1,k+1} - \varphi_{1,k}\right) \\
&\quad - \frac{1}{\beta_{1,k-1}}\left(\varphi_{e,1,k-1} + \varphi_{1,k} - \varphi_{1,k-1}\right) - \sin\left(\varphi_{1,k} - \varphi_{1,k-1}\right) \\
&\quad + i_{c_3,1,k}\sin\left(\varphi_{1,k+1} - \varphi_{1,k}\right) - i_{c_3,1,k-1}\sin\left(\varphi_{1,k} - \varphi_{1,k-1}\right) \\
-\dot{\varphi}_{1,N} + 2\dot{\varphi}_{1,N+1} &= \frac{i_b}{2} - \frac{1}{\beta_{1,N}}\left(\varphi_{e,1,N} + \varphi_{1,N+1} - \varphi_{1,N}\right) \\
&\quad - \sin\left(\varphi_{1,N+1}\right) - i_{c_3,1,N}\sin\left(\varphi_{1,N+1} - \varphi_{1,N}\right) \\
-\frac{\dot{\varphi}_{j-1,1}}{2} - \frac{\dot{\varphi}_{j-1,2}}{4} + 2\dot{\varphi}_{j,1} - \dot{\varphi}_{j,2} &= \frac{1}{\beta_{j,1}}\left(\varphi_{e,j,1} + \varphi_{j,2} - \varphi_{j,1}\right) - \sin\left(\varphi_{j,1}\right) + \frac{1}{2}\sin\left(\varphi_{j-1,1}\right) \\
&\quad + \frac{1}{4}\sin\left(\varphi_{j-1,2}\right) + i_{c_3,j,1}\sin\left(\varphi_{j,2} - \varphi_{j,1}\right) \\
3\dot{\varphi}_{j,k} - \frac{\dot{\varphi}_{j-1,k}}{2} - \frac{\dot{\varphi}_{j-1,k+1}}{4} & \\
-\frac{\dot{\varphi}_{j-1,k-1}}{4} - \dot{\varphi}_{j,k+1} - \dot{\varphi}_{j,k-1} &= \frac{1}{\beta_{j,k}}\left(\varphi_{e,j,k} + \varphi_{j,k+1} - \varphi_{j,k}\right) + \frac{1}{2}\sin\left(\varphi_{j-1,k}\right) \\
&\quad - \frac{1}{\beta_{j,k-1}}\left(\varphi_{e,j,k-1} + \varphi_{j,k} - \varphi_{j,k-1}\right)\frac{1}{4}\sin\left(\varphi_{j-1,k+1}\right) \\
&\quad - \sin\left(\varphi_{j,k}\right) + \frac{1}{4}\sin\left(\varphi_{j-1,k-1}\right) + i_{c_3,j,k}\sin\left(\varphi_{j,k+1} - \varphi_{j,k}\right) \\
&\quad - i_{c_3,j,k-1}\sin\left(\varphi_{j,k} - \varphi_{j,k-1}\right)
\end{aligned}
$$

$$
\begin{aligned}
-\frac{\dot{\varphi_{j-1,N}}}{4} - \frac{\dot{\varphi_{j-1,N+1}}}{2} & \\
+2\dot{\varphi_{j,N+1}} - \dot{\varphi_{j,N}} &= \frac{1}{\beta_{j,N}}\left(\varphi_{e,j,N} + \varphi_{j,N+1} - \varphi_{j,N}\right) + \frac{1}{2}\sin\left(\varphi_{j-1,N+1}\right) \\
&\quad - \sin\left(\varphi_{j,N+1}\right) + \frac{1}{4}\sin\left(\varphi_{j-1,N}\right) \\
&\quad - i_{c_3,j,N}\sin\left(\varphi_{j,N+1} - \varphi_{j,N}\right)
\end{aligned}
$$

Where $j = 2 : M$, $k = 2 : N$, the $i_{c_3,j,k} = 0.25$ mA, M and N indicate the SQUID in the array. The voltage response is calculated by

$$
V(\tau) = \sum_{j=1}^{M}\left(\frac{\dot{\varphi_{j,1}} + \varphi_{j,N+1}}{2}\right) \tag{2-9}
$$

where

$$
\tau = \omega_c t = \frac{2eI_cR_N}{\hbar}t. \tag{2-10}
$$

Where

$$
\begin{aligned}
I_c &\approx 0.25mA \\
R_N &\approx 2.4\Omega \\
V_c &= I_cR_n \\
\Phi_0 &= \frac{h}{2e}Wb \\
h &= 6.6260696 \times 10^{-34}Js \\
\hbar &= \frac{h}{2\pi}Js \\
e &= 1.6021766 \times 10^{-19}C
\end{aligned}
$$

$$\omega_c = \frac{2eI_cR_N}{\hbar} = \frac{2\pi V_c}{\Phi_0} = 1.8231208\frac{1}{s} \tag{2-11}$$

$$V(t) = I_cR_N\frac{\dot{\varphi}_1 + \dot{\varphi}_2}{2}V \tag{2-12}$$

$$\omega_c\dot{\varphi}_i = \frac{2e}{\hbar}. \tag{2-13}$$

The voltage input/output relationship is numerically determined by running a test frequency of 3 MHz through the model and creating a plot of the output response when the signal strength is increases from 10^{-6} to 10^{6} to produce a dynamic range plot as presented in Figure 10. The dynamic range plot shows a linear range from 0.00267 V_{p-p} to 0.1747 V_{p-p}. The input voltage V_{p-p} = 0.02V is used to generate frequency response of the transfer function.

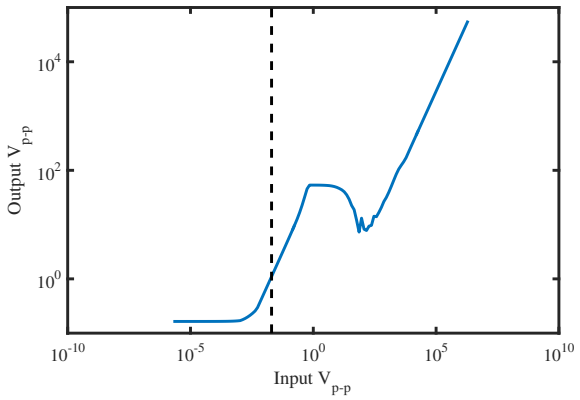

Figure 10. V_{p-p} **In vs.** V_{p-p} **Out for the 2D Bi-SQUID model used at** 3**MHz**

The frequency response of the 2D-Bi-SQUID array shows an antenna gain of 49.08 dBi at 3 MHz and 48.8 dBi at 30 MHz as seen in Figure 11.

Comparing the gain versus frequency response of the 2D Bi-SQUID with the frequency response shown in Archer's work [3] and seen in Figure 12, suggests a possibility of more then 100 dB of gain improvement over the B-dot sensor. The

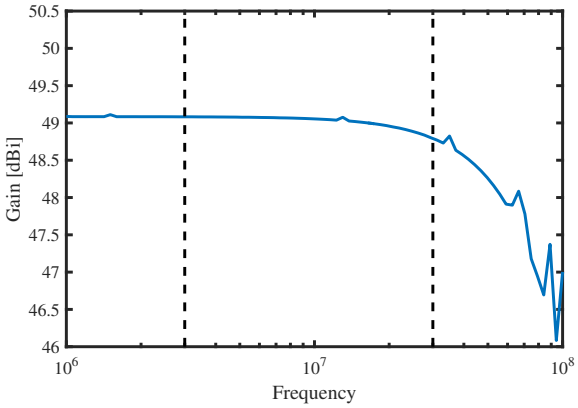

Figure 11. Frequency vs. Gain for the 2D Bi-SQUID model used

massive gain difference along with a near elimination of cross-coupling, low thermal and sensor noise provides information supporting use of the 2D Bi-SQUID sensor as an improved HFDF sensor.

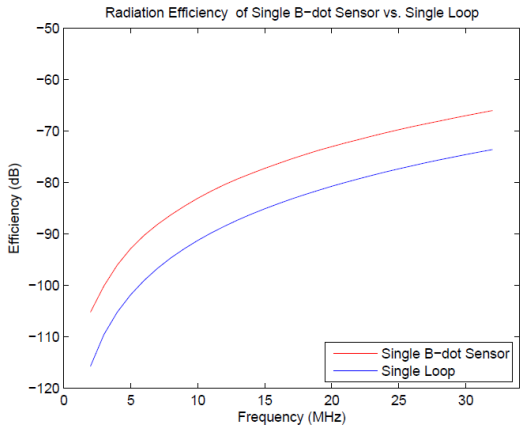

Figure 12. Frequency vs. Gain for the B-dot sensor and a metal loop antenna [3]

Traditional Poynting vector sensors have significant cross coupling between the orthogonal component sensors [15]. SQUID arrays do not have the cross coupling issue due to their small size, the intra-SQUID array cross coupling is considered insignificant beyond the adjacent SQUID. Given the devices are sharing a Josephson junction, the cross coupling between SQUID array sensors would be virtually nonexistent [1].

2.5 Conclusion

In this work 2D Bi-SQUID arrays will be used as non-linear phased array antenna elements to improve the sensitivity of the necessarily electrically small sensor, and as the magnetic field sensors for the vector sensor configuration. In chapter 3 we explore the algorithms used to estimate the Angle of Arrival (AoA) of incoming signals.

III. Methodology

3.1 Introduction

This chapter introduces Direction Finding (DF) techniques and describes two algorithms used to estimate the Angle of Arrival (AoA) of signals in a simulated environment. The performance of these two methods will be used to evaluate the utility of 2D Bi-Superconducting Quantum Interference Devices (Bi-SQUIDs) in Chapter 4 where the performance of the Superconducting Quantum Interference Devices (SQUIDs) is compared to a typical electrically small antenna. In the simulations the sensor elements are 2D Bi-SQUIDs as described earlier. The simulated elements are placed in positions determined by BerrieHill Research Corporation (BRC) during an optimization for High Frequency Direction Finding (HFDF) on a RC-135 air frame shown in Figure 13 [16, 4]. The first technique explored is beamforming. The beamforming technique is reduced to the non-uniform array Multi-Signal Classification (MUSIC) algorithm. The MUSIC algorithm is chosen because of reduced computational complexity when exploring multiple targets. The reduced computational complexity makes the non-uniform array MUSIC approach a viable solution in a real-world system. The second technique is the Poynting vector method using the Estimation of Signal Parameters via Rotational Invariance Techniques (ESPRIT) algorithm. These two methods are selected due to the nature of the associated algorithms. The beamforming technique relies on element spacing which must be matched to frequency length; whereas the Poynting vector method is agnostic to wavelength as long as the antenna element is electrically small to the wavelength of the signal. The signals processed by the algorithm are generated through a MATLAB® script provided by Space and Naval Warfare Systems Command (SPAWAR) which is modified to take an input of magnetic flux signals, and provides an output voltage for the algorithms to work on.

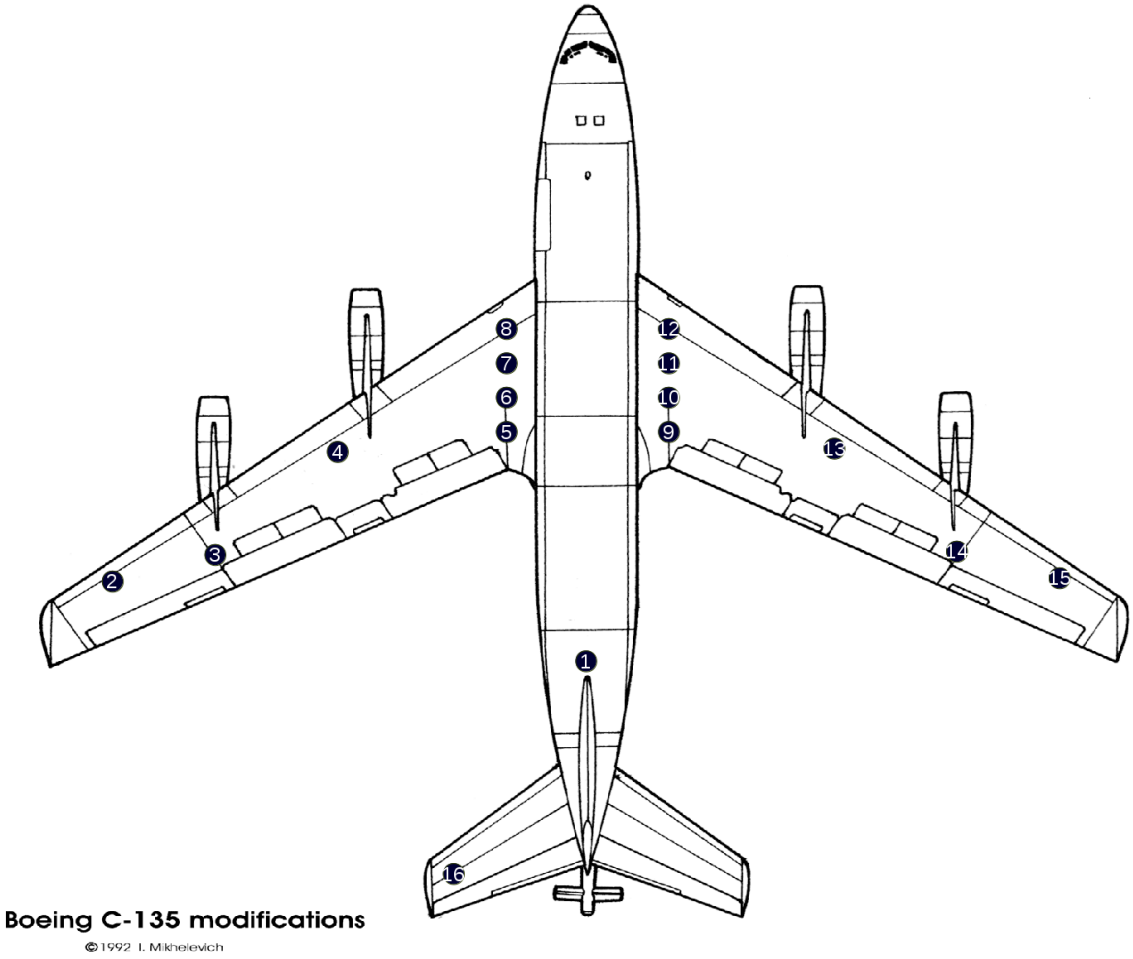

Figure 13. Sensor Placement on an RC-135

Table 1. SQUID Sensor Array Element Position in meters

$Sensor$	x_i	y_i	z_i
1	0	0	0
2	21.476	3.591	0
3	16.836	4.976	0
4	11.262	9.578	0
5	3.592	10.289	0
6	3.592	11.860	0
7	3.592	13.394	0
8	3.592	14.928	0
9	−3.592	14.928	0
10	−3.592	13.394	0
11	−3.592	11.860	0
12	−3.592	10.289	0
13	−11.262	9.578	0
14	−16.836	4.976	0
15	−21.476	3.591	0
16	6.024	−9.579	0

3.2 Assumptions

The assumptions used in this thesis are chosen to simplify the math and the computational complexity of the computer simulation. The first assumption is that each SQUID array sensor is located in loss-less homogeneous free space. This means that multipath is not considered, nor is the influence of the platform on which the sensor is mounted considered. The second is that each sensor does not couple beyond the coupling occurring within the individual SQUID array sensors. Finally, the Earth's magnetic field is also neglected.

3.3 Direction Finding

Initial DF methods, referred to as monopulse, used two antennas slightly offset from each other and used the difference of the two signals return power to drive the antenna pair to physically point at the target. This method is effective for single targets. This method is still used in many radar-guided ordinance and other simple

radar based tracking systems [17].

More recent methods that utilize an antenna array use a form of matched filtering to check the incoming signal against the hermitian, or complex conjugate, of the expected response from all possible angles. In Subsection 3.4.2, one such phased array based method is expanded from the computationally complex and time consuming method beam forming, to the simplified and much faster MUSIC algorithm to resolve the direction of $N-1$ signals. Where N is the number of antenna array elements [18].

Other methods exploit Poynting's theorem. The Poynting based methods require a minimum of three mutually orthogonal antenna elements to resolve an estimate of the AoA. The mutually orthogonal electric field vector sensor elements are referred to as a dipole triad. The standard device used to collect the magnetic field component for vector sensor is three mutually orthogonal loop antennas called a loop triad [19]. The dipole triad and loop triad are typically colocated. Using both a dipole triad and loop triad provides additional accuracy in AoA estimation. The loop antennas read the magnetic field induced current off the loop. The loop antenna elements are effective, but are not as sensitive as SQUID based sensors [3].

The normally colocated sensors can be distributed linearly for the electromagnetic component, for example the electrical dipole sensors are linearly distributed and the magnetic loops are linearly distributed [15]. The advantage of this implementation of the vector sensor is that mutual coupling is significantly reduced, and the increased size in aperture improves AoA angular resolution. The magnetic loop sensor line is parallel to the electric dipole line as shown in Fig 14. Additionally the spacing between the x-axis oriented dipole and the y-axis oriented dipole must be the same as the distance between the x-axis oriented loop and the y-axis oriented loop. The distance between the y-axis oriented dipole and the z-axis oriented dipole must be the

same as the distance between the y-axis oriented loop and the z-axis oriented loop. The distributed vector sensor approach is further explored in Subsection 3.5.3.

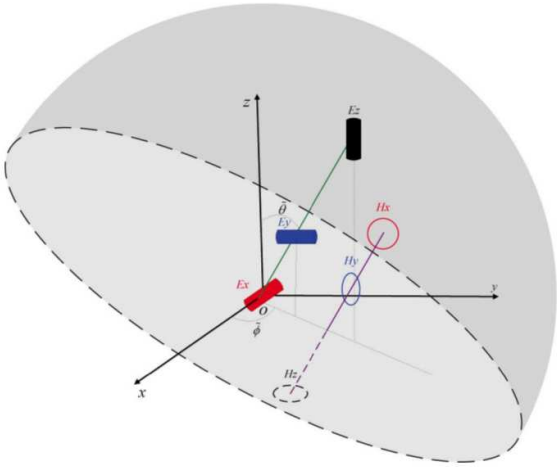

Figure 14. The Non-Colocated Vector Sensor elements are arranged such that all the electric field sensors lie on the same line, and all the magnetic field sensors lie on a separate line parallel to the electric field sensor line [15].

3.4 Method 1: Signal Model

The model starts with the received signal. The array is assumed uniform and planar until the model is expanded into the nonuniform array model at the end of this section. The received signal is a time delayed version of the transmitted signal as seen in (3-1). Where $\mathbf{x}(t)$ is the vector of the incident planar pass-band signal on the array [18].

$$\mathbf{x}(t) = \begin{bmatrix} s(t-\tau_1)\, e^{jw_c(t-\tau_1)} \\ s(t-\tau_2)\, e^{jw_c(t-\tau_2)} \\ \vdots \\ s(t-\tau_M)\, e^{jw_c(t-\tau_M)} \end{bmatrix} \tag{3-1}$$

Where

$m \triangleq \{1, 2, \ldots, M\}$, M being the number of incident antenna elements

$\tau_m \triangleq$ propagation time delay

$w_c \triangleq$ angular frequency in radians of the carrier wave

$s(t) \triangleq$ baseband signal transmitted

The angular carrier frequency is related to carrier frequency by [18]

$$w_c = 2\pi f_c. \tag{3-2}$$

Where f_c is the carrier frequency of the signal incident on the array. The propagation delay from transmission of the signal until it arrives at the m^{th} element is given by

$$\tau_m = \tau_0 - \left(\frac{d_m}{c}\right) \sin\theta. \tag{3-3}$$

Where

$\tau_0 \triangleq$ the propagation time from transmitter to a reference element on the antenna array

$\theta \triangleq$ the signal AoA with reference to the normal of the antenna array

$d_m \triangleq$ distance the m^{th} element is from the reference element in the array

When setting an array element as a reference element τ_0 can be set to zero. Setting $\tau_0 = 0$ results in [18]

$$\tau_m = -\left(\frac{d_m}{c}\right) \sin\theta. \tag{3-4}$$

In (3-3) the τ_0 term contributes the phase term $e^{-jw_c\tau_0}$, by setting $\tau_0 = 0$ a random phase term is introduced to each signal. The random phase term is constant across each element for each signal. Converting (3-1) to baseband gives [18]:

$$\mathbf{x}(t) = \begin{bmatrix} s(t-\tau_1)\, e^{jw_c\tau_1} \\ s(t-\tau_2)\, e^{jw_c\tau_2} \\ \vdots \\ s(t-\tau_M)\, e^{jw_c\tau_M} \end{bmatrix} \tag{3-5}$$

The signal vector (3-5) can be further reduced when considering a narrowband signal. This is shown by considering the time it takes the plane wave to travel across the aperture [18] given as:

$$\frac{D\lambda}{c} = \frac{D}{f_c} \tag{3-6}$$

Where

$\lambda \triangleq$ the wavelength in meters

$D \triangleq$ the aperture of the array in wavelengths

$f_c \triangleq$ the carrier frequency of the signal incident on the array

The travel time τ_m must be such that [18]

$$\tau_m < \frac{D}{f_c} \tag{3-7}$$

The signal bandwidth must be

$$B \ll \frac{f_c}{D} \tag{3-8}$$

The bandwidth to aperture relation (3-8) implies that the signal is a narrowband signal. The narrowband assumption allows [18]

$$s\left(t-\tau_m\right) \approx s\left(t\right) \tag{3-9}$$

Which further simplifies (3-5) to

$$\mathbf{x}\left(t\right) = s\left(t\right) \begin{bmatrix} e^{jw_c\tau_1} \\ e^{jw_c\tau_2} \\ \vdots \\ e^{jw_c\tau_M} \end{bmatrix} \tag{3-10}$$

Assuming an unit amplitude signal $s\left(t\right) = 1$ the "array manifold" can be written as [18]

$$\mathbf{a}\left(\theta\right) = \begin{bmatrix} e^{j2\pi d_1 \sin\theta/\lambda} \\ e^{j2\pi d_2 \sin\theta/\lambda} \\ \vdots \\ e^{j2\pi d_M \sin\theta/\lambda} \end{bmatrix} \tag{3-11}$$

The final signal that is received by the DF algorithm is given by

$$\mathbf{y}\left(t\right) = \left(\sqrt{SNR}\right) s\left(t\right) \mathbf{a}\left(\theta_0\right) + \mathbf{v}\left(t\right) \tag{3-12}$$

Where

$$\begin{aligned} SNR &\triangleq \text{the signal-to-noise ratio} \\ \mathbf{v}\left(t\right) &\triangleq \text{vector of zero-mean unit-variance Gaussian noise} \end{aligned} \tag{3-13}$$

Using instantaneous snapshots to define discrete samples of the received signal (3-12) becomes

$$\mathbf{y}[k] = \left(\sqrt{SNR}\right) s[k]\, \mathbf{a}(\theta_0) + \mathbf{v}[k] \tag{3-14}$$

Where $\mathbf{v}[k]$ is assumed to be independent and identically distributed Gaussian between snapshots.

3.4.1 Method 1: Beam Forming AoA Estimation.

Delay-sum beamforming uses time, or phase delays, to align the phase term $e^{jw_c\tau_m}$ of each element. The aligning results in a gain when all elements are combined. This is most apparent in (3-10) where all phase vectors are pointed in the same direction, and the combination is purely constructive. The result of a purely constructive combination is a gain peak in the direction the signal originated from. The AoA spectrum given by (3-15) is maximized when $\theta = \theta_0$ indicating the AoA. Any phase variation would result in smaller return. This phase relationship is exploited to determine the AoA [18].

$$\left|\mathbf{a}^H(\theta)\, \mathbf{a}(\theta_0)\right| \tag{3-15}$$

Where

$$\begin{aligned} \theta &\triangleq \text{the guessed AoA} \\ \theta_0 &\triangleq \text{the true AoA} \\ (\cdot)^H &\triangleq \text{the hermetian transpose} \\ |\cdot| &\triangleq \text{the magnitude of the contents} \end{aligned}$$

Replacing the array manifold vector $\mathbf{a}^H(\theta)$ with the weighting vector $\mathbf{W}^H(\theta)$, and as before assuming a unit power signal gives [18]

$$p(\theta) = \left|\mathbf{W}^H(\theta)\,\mathbf{a}(\theta_0)\right|^2 \tag{3-16}$$

Equation (3-16) is the general form of the Maximum Likelihood Estimator (MLE) of the single AoA azimuth direction component θ. To account for noise the Signal to Noise Ratio (SNR) can be used to scale the calculated power [18].

$$p(\theta) = SNR\left|\mathbf{W}^H(\theta)\,\mathbf{a}(\theta_0)\right|^2 \tag{3-17}$$

To make the noise power at the beamformer output the same as the antenna element output we scale the array manifold by the magnitude of the array manifold as seen below [18].

$$\mathbf{W}(\theta) = \frac{\mathbf{a}(\theta)}{|\mathbf{a}(\theta)|} \tag{3-18}$$

3.4.2 Method 1: Co-Channel Emitters Beam Forming AoA Estimation.

Expanding the signals to multiple signals sharing the same channel or frequency changes (3-12) to [18]

$$\mathbf{y} = \alpha_0\mathbf{a}(\theta_0) + \alpha_1\mathbf{a}(\theta_1) + \mathbf{v} \tag{3-19}$$

For P signals (3-19) becomes

$$\mathbf{y} = \sum_{p=1}^{P}\alpha_p\mathbf{a}(\theta_p) + \mathbf{v} \tag{3-20}$$

The form of the MLE method does not change regardless of the number of signals. The ability to resolve all signals is bound by the number of sensors, but the incoming signal is the sum of all signals present at a given location. The MLE algorithm is computationally expensive because it requires an exhaustive search of the entire angular space for each signal present. Given a search area of 180 deg azimuth and 180 deg elevation using a search resolution of 1 deg would result in the interrogation of 32400 points. To reduce the computation time of the AoA estimation we turn to the MUSIC algorithm. The MUSIC algorithm estimates the AoA of P signals using K sensors. The algorithm requires that $K \geq P + 1$ to resolve the location of each signal [18]. The received signal at each sensor is described by (3-21).

$$\mathbf{y}[k] = \sum_{p=1}^{P} \alpha_p[k]\, \mathbf{a}(\theta_p) + \mathbf{v}[k] \tag{3-21}$$

where,

$$k = 1, \ldots K, \text{ where } K \text{ is the total number of signal samples} \tag{3-22}$$

$$\theta_p \triangleq \text{signal directions} \tag{3-23}$$

$$\alpha_p[k] \triangleq \text{complex amplitudes of the signals} \tag{3-24}$$

$$\mathbf{v}[k] \triangleq \text{vector of zero-mean unit-variance Gaussian noise} \tag{3-25}$$

The formulation for MUSIC begins with the co-variance $\mathbf{R}_y = E\left\{\mathbf{y}[k]\,\mathbf{y}^H[k]\right\}$ given by [18]

$$\mathbf{R}_y = \sum_{p=0}^{P} \sigma_p^2 \mathbf{a}(\theta_p)\, \mathbf{a}^H(\theta_p) + \mathbf{I} \tag{3-26}$$

Where the SNR of the p^{th} signal is given by [18]

$$\sigma_p^2 = E\left\{\left|\alpha_p\left[k\right]\right|^2\right\} \tag{3-27}$$

The co-variance can be decomposed into eigenvalues and eigenvectors by the following singular-value decomposition [18]

$$\mathbf{R}_y = \mathbf{U}\mathbf{\Sigma}\mathbf{U}^H \tag{3-28}$$

Where the singular values of $\mathbf{R}_y$ are contained in the diagonal of [18]

$$\mathbf{\Sigma} = diag\left\{\left[\sigma_1^2 + 1, \ldots, \sigma_P^2 + 1, 1, \ldots, 1\right]\right\} \tag{3-29}$$

$\mathbf{U}$ is the matrix of singular vectors which can be further divided into the two matrices [18]

$$\mathbf{U} = \left[\mathbf{U}_s, \mathbf{U}_n\right] \tag{3-30}$$

$\mathbf{U}_s$ is $M \times P$ singular vectors corresponding to the P largest singular values. $\mathbf{U}_s$ is called the signal subspace. $\mathbf{U}_n$ is $M \times M - P$ singular vectors corresponding to the $M - P$ smallest singular values. $\mathbf{U}_n$ is called the noise subspace. $\mathbf{U}$ is a unitary matrix which means that $\mathbf{U}_s$ and $\mathbf{U}_n$ are orthogonal.

$$\mathcal{R}\left\{\mathbf{U}_s\right\} = \left[a\left(\theta_1\right), \ldots, a\left(\theta_P\right)\right] \tag{3-31}$$

Where

$$\mathcal{R}\left\{\cdot\right\} \triangleq \text{the Range of the subspace} \tag{3-32}$$

Since $\mathbf{U}_s$ and $\mathbf{U}_n$ are orthogonal [18]

$$\mathbf{U}_s^H \mathbf{U}_n = 0 \tag{3-33}$$

Equation (3-33) allows for the exploitation of the smaller noise subspace or null space which results in [18]

$$\mathbf{a}^H(\theta)\,\mathbf{U}_n = 0 \text{ , for } \theta = \theta_1, \ldots, \theta_P \tag{3-34}$$

The MUSIC spectrum is thus defined as

$$S(\theta) = \frac{1}{\left|\mathbf{a}^H(\theta)\,\mathbf{U}_n\right|^2}. \tag{3-35}$$

In the real world $\mathbf{R}_y$ can not be known prior to receiving the signal, but the co-variance matrix can be estimated by [18]

$$\hat{\mathbf{R}}_y = \sum_{k=1}^{K} \mathbf{y}[k]\,\mathbf{y}^H[k] \tag{3-36}$$

Using the estimated covariance matrix $\hat{\mathbf{R}}_y$ gives

$$\hat{\mathbf{R}}_y = \hat{\mathbf{U}}\hat{\mathbf{\Sigma}}\hat{\mathbf{U}}^H \tag{3-37}$$

Where $\hat{\mathbf{U}} = \left[\hat{\mathbf{U}}_s, \hat{\mathbf{U}}_n\right]$ which gives the estimated MUSIC Spectrum

$$\hat{S}(\theta) = \frac{1}{\left|\mathbf{a}^H(\theta)\,\hat{\mathbf{U}}_n\right|^2} \tag{3-38}$$

The maximum is calculated from (3-38) resulting in the estimated AoA or $\hat{\theta}$.

3.4.3 Method 1: Non-Uniform Co-Channel Emitters Beam Forming AoA Estimation.

The AoA of L signal azimuth and elevation pairs are represented as the angle pairs, $(\theta_1, \phi_1), \ldots, (\theta_L, \phi_L)$. Considering N non-uniformly spaced array elements and the k^{th} snapshot provides [18]

$$x(k) = \mathbf{A}(\theta)\,\mathbf{s}(k) + \mathbf{n}(k) \tag{3-39}$$

Where

$$\begin{aligned} \theta &= [\theta_1, \phi_1, \ldots, \theta_L, \phi_L]^T && (3\text{-}40)\\ \mathbf{A}(\theta) &= [\mathbf{a}(\theta_1, \phi_1), \ldots, \mathbf{a}(\theta_L, \phi_L)] && (3\text{-}41)\\ \mathbf{s}(k) &\triangleq L \times 1 \text{ signal vector} \\ \mathbf{n}(k) &\triangleq N \times 1 \text{ noise vector} \end{aligned}$$

Where θ is a $2N \times 1$ vector of AoA angles, $\mathbf{A}(\theta)$ is the $N \times L$ signal direction matrix, and the $N \times 1$ steering vector is given by

$$\mathbf{a}(\theta, \phi) = \begin{bmatrix} \exp\left\{ j\frac{2\pi}{\lambda}\left(x_1 \sin\theta \sin\phi + y_1 \cos\theta \sin\phi + z_1 \cos\phi\right)\right\} \\ \vdots \\ \exp\left\{ j\frac{2\pi}{\lambda}\left(x_N \sin\theta \sin\phi + y_N \cos\theta \sin\phi + z_N \cos\phi\right)\right\} \end{bmatrix} \tag{3-42}$$

Where the sensor coordinates are given by $\{x_i, y_i, z_i\}$ seen in Figure 2.

The co-variance $\mathbf{R}_x = E\left\{\mathbf{x}(k)\,\mathbf{x}^H(k)\right\}$ is given by

$$\mathbf{R}_x = \mathbf{A}\mathbf{R}_s\mathbf{A}^H + \sigma^2\mathbf{I}_N \tag{3-43}$$

Where

$$\begin{aligned} \mathbf{I}_N &\triangleq \text{an } N \times N \text{identity matrix} \\ \sigma^2 &\triangleq \text{the element noise variance} \end{aligned}$$

$$\mathbf{R}_s = E\left\{\mathbf{s}\left(k\right)\mathbf{s}^H\left(k\right)\right\} \tag{3-44}$$

The eigendecomposition of R_x gives

$$\mathbf{R}_x = \sum_{k=1}^{N} \lambda_k \mathbf{e}_k \mathbf{e}_k^H \tag{3-45}$$

Where

$$\begin{aligned} \lambda_k &\triangleq k^{th} \text{ eigenvalue corresponding to } \mathbf{R}_x \\ \mathbf{e}_k &\triangleq k^{th} \text{eigenvector associated with the } k^{th} \text{ eigenvalue} \end{aligned}$$

The eigenvalues λ_k are sorted in descending order ($\lambda_1 \geq \lambda_2 \geq \cdots \geq \lambda_N$).

$$\begin{aligned} \mathbf{E}_s &\triangleq [\mathbf{e}_1, \ldots, \mathbf{e}_L] \\ \mathbf{E}_N &\triangleq [\mathbf{e}_{L+1}, \ldots, \mathbf{e}_N] \end{aligned}$$

$\mathbf{E}_s$ is the signal-subspace of L eigenvectors.

$\mathbf{E}_N$ is the noise-subspace of $N - L$ eigenvectors

As before, the co-variance $\mathbf{R}_x$ can not be known prior to receiving the signal, but the co-variance can be estimated by

$$\hat{\mathbf{R}}_x = \frac{1}{K}\sum_{k=1}^{K}\mathbf{x}\left(k\right)\mathbf{x}^H\left(k\right) \tag{3-46}$$

where K is the number of snapshots

The eigendecomposition of the estimated co-variance gives

$$\hat{\mathbf{R}}_x = \hat{\mathbf{E}}_s\hat{\mathbf{\Lambda}}_s\hat{\mathbf{E}}_s^H + \hat{\mathbf{E}}_N\hat{\mathbf{\Lambda}}_N\hat{\mathbf{E}}_N^H \tag{3-47}$$

Where

$$\hat{\mathbf{E}}_s \triangleq [\hat{e}_1, \ldots, \hat{e}_L] \tag{3-48}$$

$$\hat{\mathbf{E}}_N \triangleq [\hat{e}_1, \ldots, \hat{e}_N] \tag{3-49}$$

$$\hat{\mathbf{\Lambda}}_s \triangleq diag\left\{\hat{\lambda}_1, \ldots, \hat{\lambda}_L\right\} \tag{3-50}$$

$$\hat{\mathbf{\Lambda}}_N \triangleq diag\left\{\hat{\lambda}_{L+1}, \ldots, \hat{\lambda}_N\right\} \tag{3-51}$$

The MUSIC null spectrum formula is then

$$f\left(\theta,\phi\right) = \mathbf{a}^H\left(\theta,\phi\right)\hat{\mathbf{E}}_N\hat{\mathbf{E}}_N^H\mathbf{a}\left(\theta,\phi\right) = \left\|\hat{\mathbf{E}}_N^H\mathbf{a}\left(\theta,\phi\right)\right\|^2 \tag{3-52}$$

Where $\|\cdot\|$ is the vector 2 norm. The maximum is calculated from (3-52) resulting in the estimated AoA or $\hat{\theta}$ and $\hat{\phi}$.

3.4.4 Verification of the MUSIC algorithm implementation.

Verification of the MUSIC algorithm is accomplished using a pure tone received on a linear array that is 5λ long or 10 elements long and has an element spacing of $\frac{\lambda}{2}$. The signals are transmitted at 60 deg and 160 deg. The MUSIC spectrum output is seen in 15 shows that the algorithm is able to accurately estimate the AoA of two co-channel signals.

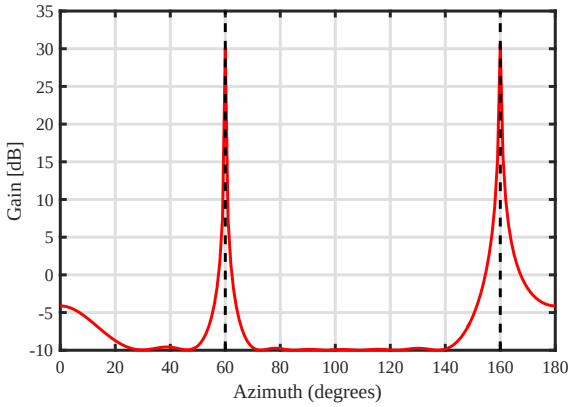

Figure 15. This plot shows the validation output using an array that is 10 elements long and each element is spaced $\frac{\lambda}{2}$ appart

3.4.5 Constraints.

The MUSIC algorithm performs optimally when the aperture is more than 1.5λ long in the dimension of interest, and has an element spacing of $\frac{\lambda}{2}$ or less. For example, if the array is designed to only look at azimuth, a linear array that is 1.5λ long or longer will work well. Additionally, the MUSIC algorithm is a narrow band algorithm. For this experiment set, each transmitted frequency is assumed known and is used as the center frequency for estimating the AoA of the signals on that channel. The final constraint is that the number of signals must be assumed.

3.5 Method 2: Poynting Vector Introduction

The Poynting Vector approach collects field information from three orthogonal antennas and processes the induced voltages to determine a vector that points in the direction of signal's source. This process ideally contains antennas that measure both electrical $\overrightarrow{\mathbf{E}}$ field and magnetic $\overrightarrow{\mathbf{H}}$ field. For this implementation, only the magnetic $\overrightarrow{\mathbf{H}}$ field is considered. To begin the development of this model a description of the electromagnetic signals is generated.

3.5.1 Method 2: Plane Wave Description.

The transmitted signal is assumed to be in the far field, meaning that the signal wave front surface curvature is asymptotically locally planar. The incoming signal wave is described as Transvers Electromagnetic (TEM) meaning that oscillations of the electric $\overrightarrow{\mathbf{E}}$ field and magnetic $\overrightarrow{\mathbf{H}}$ field are mutually orthogonal to the direction of propagation. The magnetic and electric plane wave is shown in Figure 16 and described by

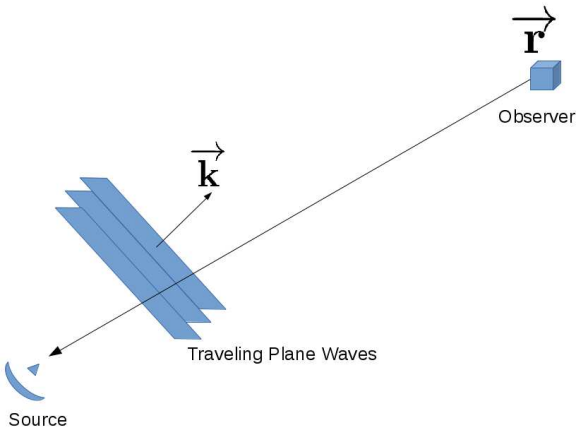

Figure 16. Graphic Description of Vectors k and r

$$\overrightarrow{\mathbf{H}} = (H_x\hat{x} + H_y\hat{y} + H_z\hat{z})\, e^{-j\overrightarrow{\mathbf{k}}\cdot\overrightarrow{\mathbf{r}}} \tag{3-53}$$

$$\overrightarrow{\mathbf{E}} = (E_x\hat{x} + E_y\hat{y} + E_z\hat{z})\, e^{-j\overrightarrow{\mathbf{k}}\cdot\overrightarrow{\mathbf{r}}}. \tag{3-54}$$

Where

$$\begin{aligned}
\overrightarrow{\mathbf{r}} &= r_x\hat{x} + r_y\hat{y} + r_z\hat{z} \text{ points from the source to the observer} && (3\text{-}55)\\
\overrightarrow{\mathbf{k}} &= k_x\hat{x} + k_y\hat{y} + k_z\hat{z} \text{ points in the direction of propagation} && (3\text{-}56)\\
\{H_x, H_y, H_z\} &\triangleq \text{magnetic vector componenet magnitude}\\
\{E_x, E_y, E_z\} &\triangleq \text{electric vector componenet magnitude}\\
\{\hat{x}, \hat{y}, \hat{z}\} &\triangleq \text{cartesian unit vectors.}
\end{aligned}$$

In Equation (3-53) and (3-54), $e^{-j\overrightarrow{\mathbf{k}}\cdot\overrightarrow{\mathbf{r}}}$ expresses the phase contribution to the traveling wave. The direct ray $\overrightarrow{\mathbf{r}}$ described in (3-55) is a vector that originates at the signal source, and points to the location of the observer. The wave number vector $\overrightarrow{\mathbf{k}}$ described in (3-56) is a vector that again originates at the signal source but points to the direction of propagation. The wave propagation vector magnitude is given by

$$\left|\overrightarrow{\mathbf{k}}\right| = \sqrt{k_x^2 + k_y^2 + k_z^2} = \frac{2\pi}{\lambda} = \omega\sqrt{\mu_0\varepsilon_0}. \tag{3-57}$$

Where

$$\begin{aligned}
\omega &= 2\pi f && (3\text{-}58)\\
\mu_0 &= 4\pi \times 10^{-}7\left[\frac{Henry}{meters}\right], \text{ is the permeability of free space.}\\
\varepsilon_0 &= \frac{1}{\mu_0 c^2}, \text{ is the permittivity of free space}\\
c &= 299,792,458\left[\frac{meters}{second}\right], \text{ is the speed of light}
\end{aligned}$$

3.5.2 Method 2: Co-located Poynting Vector AoA Estimation.

The Poynting vector has a magnitude equal to the instantaneous power of an electromagnetic (EM) wave and is pointed in the direction of energy flow. The mathematical definition is [20, p.401]

$$\overrightarrow{\mathcal{P}} \triangleq \overrightarrow{\mathbf{E}} \times \overrightarrow{\mathbf{H}}. \tag{3-59}$$

The instantaneous power from the EM signal is deposited on the vector sensor elements as described by

$$\mathbf{a} \triangleq \begin{bmatrix} \overrightarrow{\mathbf{E}} \\ \overrightarrow{\mathbf{H}} \end{bmatrix} \triangleq \begin{bmatrix} E_x \\ E_y \\ E_z \\ H_x \\ H_y \\ H_z \end{bmatrix} \triangleq \underbrace{\begin{bmatrix} \cos\phi\cos\theta & -\sin\phi \\ \sin\phi\cos\theta & \cos\phi \\ -\sin\theta & 0 \\ -\sin\phi & -\cos\phi\cos\theta \\ \cos\phi & -\sin\phi\cos\theta \\ 0 & \sin\theta \end{bmatrix}}_{\triangleq\boldsymbol{\Theta}(\theta,\phi)} \underbrace{\begin{bmatrix} \sin\gamma e^{j\eta} \\ \cos\gamma \end{bmatrix}}_{\triangleq\mathbf{g}(\gamma,\eta)}. \tag{3-60}$$

Where

$$\begin{aligned} \theta \in [0,\pi] &\triangleq \text{source elevation-angle measured from positive } z\text{-axis} \\ \phi \in [0,2\pi) &\triangleq \text{source azimuth-angle measured from positive } x\text{-axis} \\ \gamma \in \left[0,\frac{\pi}{2}\right] &\triangleq \text{auxiliary polarization} \\ \eta \in [-\pi,\pi) &\triangleq \text{polarization phase difference.} \end{aligned}$$

It is important to note that $\boldsymbol{\Theta}(\theta,\phi)$ is a function of AoA and $\mathbf{g}(\gamma,\eta)$ is a function of polarization parameters. Using the Frobenius norm denoted as $\|\cdot\|$ below we find

that

$$\left\|\overrightarrow{\mathbf{E}}\right\| = \left\|\overrightarrow{\mathbf{H}}\right\| = 1, \forall\left(\theta, \phi, \gamma, \eta\right). \tag{3-61}$$

The unit poynting vector is given by

$$\overrightarrow{\mathbf{p}} \triangleq \begin{bmatrix} p_x \\ p_y \\ p_z \end{bmatrix} = \frac{\overrightarrow{\mathbf{E}} \times \overrightarrow{\mathbf{H}}^*}{\left\|\overrightarrow{\mathbf{E}}\right\| \cdot \left\|\overrightarrow{\mathbf{H}}\right\|} = \begin{bmatrix} u \\ v \\ w \end{bmatrix} \triangleq \begin{bmatrix} \sin\theta\cos\phi \\ \sin\theta\sin\phi \\ \cos\theta \end{bmatrix}. \tag{3-62}$$

Where * represents the complex conjugate, and $\times$ indicates a vector cross-product operator.

Define $\overrightarrow{\mathbf{u}}$ as the unit vector pointing toward the source gives [21]

$$\overrightarrow{\mathbf{u}} = \begin{bmatrix} \cos\theta\cos\phi \\ \sin\theta\cos\phi \\ \sin\phi \end{bmatrix} = -\overrightarrow{\mathbf{p}}. \tag{3-63}$$

Next the colocated vector sensor component sensors are separated to reduce element cross coupling and improve resolution for a portion of the High Frequency (HF) band.

3.5.3 Method 2: Non-Colocated Poynting Vector AoA Estimation.

The co-located Poynting vector method does not take into consideration element cross coupling which occurs when elements are near other elements or are co-located. The cross coupling can be removed by spacing the elements out. Incorporating the displacement in equation (3-60) results in [15]

$$\tilde{\mathbf{a}} \triangleq \begin{bmatrix} \tilde{\mathbf{E}} \\ \tilde{\mathbf{H}} \end{bmatrix}$$

$$\triangleq \underbrace{\begin{bmatrix} 1 \\ e^{-j\frac{2\pi}{\lambda}\Delta_{x,y}(\tilde{u}u+\tilde{v}v+\tilde{w}w)} \\ e^{-j\frac{2\pi}{\lambda}[\Delta_{x,y}(\tilde{u}u+\tilde{v}v+\tilde{v}w)+\Delta_{y,z}(\tilde{u}u+\tilde{v}v+\tilde{w}w)]} \\ e^{-j\frac{2\pi}{\lambda}(x_h u+y_h v+z_h w)} \\ e^{-j\frac{2\pi}{\lambda}(x_h u+y_h v+z_h w)}e^{j\frac{2\pi}{\lambda}\Delta_{x,y}(\tilde{u}u+\tilde{v}v+\tilde{w}w)} \\ e^{-j\frac{2\pi}{\lambda}(x_h u+y_h v+z_h w)}e^{j\frac{2\pi}{\lambda}[\Delta_{x,y}(\tilde{u}u+\tilde{v}v+\tilde{w}w)+\Delta_{y,z}(\tilde{u}u+\tilde{v}v+\tilde{w}w)]} \end{bmatrix}}_{\triangleq \mathbf{d}(\theta,\phi)} \odot \underbrace{\begin{bmatrix} E_x \\ E_y \\ E_z \\ H_x \\ H_y \\ H_z \end{bmatrix}}_{\mathbf{a}}. \qquad (3\text{-}64)$$

Where

$$\begin{aligned} \tilde{p_x} &= \sin\left(\tilde{\theta}\right)\cos\left(\tilde{\phi}\right) \\ \tilde{p_y} &= \sin\left(\tilde{\theta}\right)\sin\left(\tilde{\phi}\right) \\ \tilde{p_z} &= \cos\left(\tilde{\theta}\right) \\ \tilde{\theta} &\triangleq \text{elevation angle of the vector the elements are aligned on} \\ \tilde{\phi} &\triangleq \text{azimuth angle of the vector the elements are aligned on,} \end{aligned}$$

and $\odot$ is an element-wise multiplication operator.

The new cross product relationship for the distributed configuration is given by

[15]

$$\left(c\tilde{\mathbf{E}}\right)\times\left(c\tilde{\mathbf{H}}\right)^{*} = \left|c\right|^{2} \quad e^{j\frac{2\pi}{\lambda}(x_h u+y_h v+z_h w)} \begin{bmatrix} u & e^{-j\frac{2\pi}{\lambda}[(2\Delta_{x,y}+\Delta_{y,z})(\tilde{u}u+\tilde{v}v+\tilde{w}w)]} \\ v & e^{-j\frac{2\pi}{\lambda}[(\Delta_{x,y}+\Delta_{y,z})(\tilde{u}u+\tilde{v}v+\tilde{w}w)]} \\ w & e^{-j\frac{2\pi}{\lambda}[\Delta_{x,y}(\tilde{u}u+\tilde{v}v+\tilde{w}w)]} \end{bmatrix} \tag{3-65}$$

Normalize by the Frobenius norm gives

$$\begin{aligned} \frac{\left(c\tilde{\mathbf{E}}\right)\times\left(c\tilde{\mathbf{H}}\right)^{*}}{\left\|\left(c\tilde{\mathbf{E}}\right)\times\left(c\tilde{\mathbf{H}}\right)^{*}\right\|} &= e^{j\frac{2\pi}{\lambda}(x_h u+y_h v+z_h w)} \begin{bmatrix} u & e^{-j\frac{2\pi}{\lambda}[(2\Delta_{x,y}+\Delta_{y,z})(\tilde{u}u+\tilde{v}v+\tilde{w}w)]} \\ v & e^{-j\frac{2\pi}{\lambda}[(\Delta_{x,y}+\Delta_{y,z})(\tilde{u}u+\tilde{v}v+\tilde{w}w)]} \\ w & e^{-j\frac{2\pi}{\lambda}[\Delta_{x,y}(\tilde{u}u+\tilde{v}v+\tilde{w}w)]} \end{bmatrix} \\ &\triangleq \overrightarrow{\mathbf{q}} \end{aligned} \tag{3-66}$$

Equation (3-66) can be simplified by assuming that the elements are aligned along one of the Cartesian unit vectors $\hat{x}$, $\hat{y}$,or $\hat{z}$. Assuming that the elements are aligned along $\hat{x}$ translates to $\tilde{\theta}=\frac{\pi}{2}$ and $\tilde{\phi}=0$ which results in [15]

$$\overrightarrow{\mathbf{q}}_x \triangleq e^{j\frac{2\pi}{\lambda}x_h p_x} \begin{bmatrix} u & e^{-j\frac{2\pi}{\lambda}(2\Delta_{x,y}+\Delta_{y,z})u} \\ v & e^{-j\frac{2\pi}{\lambda}(\Delta_{x,y}+\Delta_{y,z})u} \\ w & e^{-j\frac{2\pi}{\lambda}\Delta_{x,y}+u} \end{bmatrix} \tag{3-67}$$

For the first of two disjoint cases where $\phi\in\left[-\frac{\pi}{2},\frac{\pi}{2}\right]$, $u\geq 0, \forall\theta\in[0,\pi]$ and so [15]

$$\overrightarrow{\mathbf{q}}_x e^{-j\angle\left[\overrightarrow{\mathbf{q}}_x\right]_1} = \begin{bmatrix} u & 0 \\ v & e^{j\frac{2\pi}{\lambda}\Delta_{x,y}u} \\ w & e^{j\frac{2\pi}{\lambda}(\Delta_{x,y}+\Delta_{y,z})u} \end{bmatrix} \triangleq \mathbf{q}'_x. \tag{3-68}$$

Where $\angle$ is the angle of the element described by $[\cdot]_i$ where i denotes the element of the vector $[\cdot]$. Breaking (3-68) into individual equations and solving for the unit estimated values of $\hat{u}$, $\hat{v}$, and $\hat{w}$ gives

$$\begin{aligned} \hat{u}_{coarse} &= \left[\mathbf{q}'_x\right]_1, \\ \hat{v} &= \mathrm{Re}\left\{\left[\mathbf{q}'_x\right]_2 e^{-j\frac{2\pi}{\lambda}\Delta_{x,y}\hat{u}_{course}}\right\}, \\ \hat{w} &= \mathrm{Re}\left\{\left[\mathbf{q}'_x\right]_3 e^{-j\frac{2\pi}{\lambda}(\Delta_{x,y}+\Delta_{y,z})\hat{u}_{course}}\right\} \end{aligned} \tag{3-69}$$

If the aperture is long with respect to wavelength, meaning that $\Delta_{x,y} > \lambda$, the coarse estimate can be further refined by taking advantage of the non-colocated arrangement of the sensors resulting in [15]

$$\hat{u}_{fine,1} = \frac{\lambda}{2\pi}\frac{1}{\Delta_{x,y}}\angle\left\{\frac{\left[\mathbf{q}'_x\right]_2}{\hat{v}}\right\} \tag{3-70}$$

$$\hat{u}_{fine,2} = \frac{\lambda}{2\pi}\frac{1}{(\Delta_{x,y}+\Delta_{y,z})}\angle\left\{\frac{\left[\mathbf{q}'_x\right]_3}{\hat{w}}\right\} \tag{3-71}$$

If $\Delta_{x,y}$ is longer then $\frac{\lambda}{2}$, there may be more then one solution for $\hat{u}_{fine,1}$ in equation (3-70). If it is found that $\hat{u}_{fine,1}$ has become ambiguous, $\hat{u}_{course}$ provides a less accurate but unambiguous solution [15]. This limit will not be approached when looking at the HF band because the distance $\Delta_{x,y} < 5$ meters.

The final estimate is then

$$\hat{\phi} = \arctan\left(\frac{\hat{v}}{\hat{u}}\right) \tag{3-72}$$

$$\hat{\theta} = \arccos\left(\hat{w}\right) \tag{3-73}$$

For the second disjoint case where $\phi \in \left[\frac{\pi}{2}, \frac{3\pi}{2}\right]$, $u \leq 0, \forall\theta \in [0, \pi]$ and

$$\overrightarrow{\mathbf{q}}_x e^{-j\angle\left[\overrightarrow{\mathbf{q}}_x\right]_1} = \begin{bmatrix} -u & 0 \\ -v & e^{j\frac{2\pi}{\lambda}\Delta_{x,y}u} \\ -w & e^{j\frac{2\pi}{\lambda}(\Delta_{x,y}+\Delta_{y,z})u} \end{bmatrix} \triangleq \mathbf{q}'_x, \tag{3-74}$$

$$\begin{aligned} \hat{u}_{course} &= -\left[\mathbf{q}'_x\right]_1, \\ \hat{v} &= \mathrm{Re}\left\{-\left[\mathbf{q}'_x\right]_2 e^{-j\frac{2\pi}{\lambda}\Delta_{x,y}\hat{u}_{course}}\right\}, \\ \hat{w} &= \mathrm{Re}\left\{-\left[\mathbf{q}'_x\right]_3 e^{-j\frac{2\pi}{\lambda}(\Delta_{x,y}+\Delta_{y,z})\hat{u}_{course}}\right\} \end{aligned} \tag{3-75}$$

$$\hat{\phi} = \arctan\left(\frac{\hat{v}}{\hat{u}}\right) + \pi \tag{3-76}$$

$$\hat{\theta} = \arccos\left(\hat{w}\right) \tag{3-77}$$

$$\hat{u}_{fine,1} = \frac{\lambda}{2\pi}\frac{1}{\Delta_{x,y}}\angle\left\{\frac{\left[\mathbf{q}'_x\right]_2}{\hat{v}}\right\} \tag{3-78}$$

$$\hat{u}_{fine,2} = \frac{\lambda}{2\pi}\frac{1}{(\Delta_{x,y}+\Delta_{y,z})}\angle\left\{\frac{\left[\mathbf{q}'_x\right]_3}{\hat{w}}\right\}. \tag{3-79}$$

Using a rotational transform with the Euler angles (α, β, τ) we can rotate the space of an arbitrarily oriented sensor set to be parallel to $\hat{x}$ by [15]

$$\begin{bmatrix} u \\ v \\ w \end{bmatrix} = \begin{bmatrix} \cos\tau & \sin\tau & 0 \\ -\sin\tau & \cos\tau & 0 \\ 0 & 0 & 1 \end{bmatrix} \begin{bmatrix} 1 & 0 & 0 \\ 0 & \cos\beta & \sin\beta \\ 0 & -\sin\beta & \cos\beta \end{bmatrix} \begin{bmatrix} \cos\alpha & \sin\alpha & 0 \\ -\sin\alpha & \cos\alpha & 0 \\ 0 & 0 & 1 \end{bmatrix} \begin{bmatrix} u' \\ v' \\ w' \end{bmatrix}. \tag{3-80}$$

From this point an eigen-based parameter-estimation algorithm called ESPRIT can be used to estimate the source location.

3.5.4 ESPRIT.

The ESPRIT algorithm is an eigen-based closed-form method for estimating the azimuth, elevation, and polarization of monochromatic signals incident on a single vector sensor [22]. Starting with the signals described by

$$\mathbf{z}(t) = \sum_{k=1}^{K} \sqrt{\mathcal{P}_k}\mathbf{a}_k e^{j2\pi f_k t + \epsilon_l} + \mathbf{n}(t) \tag{3-81}$$

Where

$$\begin{aligned} \mathcal{P}_k &\triangleq \text{signal strength or SNR} \\ \mathbf{a}_k &\triangleq \text{antenna manifold} \\ K &\triangleq \text{number of signals,} \\ \mathbf{n}(t) &\triangleq \text{additive noise.} \end{aligned}$$

The data sets required for ESPRIT are

$$\begin{aligned} \mathbf{z}(t) \quad &, \quad \forall n = 1, \ldots, N \\ \mathbf{z}(t + \Delta_T) \quad &, \quad \forall n = 1, \ldots, N. \end{aligned}$$

Where Δ_T is a constant time-delay between measurements. Form a new set of matrices from the array manifold by

$$
\begin{aligned}
\mathbf{A}_1 &\triangleq [\mathbf{a}_1, \ldots, \mathbf{a}_K] \\
\mathbf{A}_2 &\triangleq \left[\mathbf{a}_1 e^{j2\pi f_1 \Delta_T}, \ldots, \mathbf{a}_K e^{j2\pi f_K \Delta_T}\right] \\
\mathbf{\Phi} &\triangleq \begin{bmatrix} e^{j2\pi f_1 \Delta_T} & & \\ & \ddots & \\ & & e^{j2\pi f_K \Delta_T} \end{bmatrix}
\end{aligned}
$$

The measurements are then formed into $6 \times N$ arrays given by

$$
\begin{aligned}
\mathbf{Z}_1 &= [\mathbf{z}(t_1), \mathbf{z}(t_2), \ldots, \mathbf{z}(t_N)] \\
\mathbf{Z}_2 &= [\mathbf{z}(t_1 + \Delta_T), \mathbf{z}(t_2 + \Delta_T), \ldots, \mathbf{z}(t_N + \Delta_T)]
\end{aligned}
$$

Create the 6×6 correlation matrices

$$
\mathbf{R}_1 = \mathbf{Z}_1 \mathbf{Z}_1^H
$$

$$
\mathbf{R}_2 = \mathbf{Z}_2 \mathbf{Z}_2^H
$$

Where $[\cdot]^H$ denotes the Hermitian or complex conjugate transpose operator.

$\mathbf{E_1}$ is the $6 \times K$ signal-subspace which is comprised of K eigenvectors associated with the K largest eigenvalues of $\mathbf{R_1}$. Similarly, $\mathbf{E_2}$ is the signal-subspace associated with $\mathbf{R_2}$. From these subspaces we find a unique $K \times K$ non-singular matrix $\mathbf{T}$ such that [22]

$$\begin{aligned}\mathbf{E_1} &= \mathbf{A_1 T} \\ \mathbf{E_2} &= \mathbf{A_2 T} = \mathbf{A_1 \Phi T}\end{aligned}$$

Where, $[\Phi]_{j,j} = e^{j2\pi f_j \Delta_T}$, $j = 1, dots, K$. Additionally, a $K \times K$ matrix $\mathbf{\Psi}$ exists such that

$$\begin{aligned}\mathbf{A_1 \Phi = E_2} &\Rightarrow \mathbf{A_1 T \Psi = A_1 \Phi T} \\ &\Rightarrow \mathbf{\Psi} = \left(\mathbf{E_1}^H \mathbf{E_1}\right)^{-1} \left(\mathbf{E_2}^H \mathbf{E_2}\right) = \mathbf{T}^{-1} \mathbf{\Phi T} \\ &\Rightarrow \mathbf{\Phi} = \mathbf{T \Psi T}^{-1}\end{aligned}$$

because $\mathbf{E_1}$ and $\mathbf{E_2}$ are full rank. The array manifold $\mathbf{A_1}$ can be estimated as

$$\begin{aligned}\hat{\mathbf{A}}_1 &= [\hat{\mathbf{a}}_k, \ldots, \hat{\mathbf{a}}_k] = \mathbf{E_1 T}^{-1} = \mathbf{E_2 T}^{-1} \mathbf{\Phi}^{-1} \\ &= \frac{1}{2}\left(\mathbf{E_1 T}^{-1} + \mathbf{E_2 T}^{-1} \mathbf{\Phi}^{-1}\right)\end{aligned} \tag{3-82}$$

Using the idealized array manifold we can estimate the electromagnetic component vectors $\hat{\mathbf{e}}_1$ and $\hat{\mathbf{h}}_1$ by

$$\hat{\mathbf{a}}_k = \begin{bmatrix} \hat{\mathbf{e}}_1 \\ \hat{\mathbf{h}}_1 \end{bmatrix} \tag{3-83}$$

and estimate the Poynting vector by

$$\begin{bmatrix} \hat{u}_k \\ \hat{v}_k \\ \hat{w}_k \end{bmatrix} = \hat{\mathbf{p}}_k \triangleq \begin{bmatrix} \hat{p}_x \\ \hat{p}_y \\ \hat{p}_z \end{bmatrix} = \frac{\hat{\mathbf{e}}_k \times \hat{\mathbf{h}}_k^*}{\|\hat{\mathbf{e}}_k\| \cdot \left\|\hat{\mathbf{h}}_k\right\|}. \tag{3-84}$$

The AoA for the kth signal can be estimated by

$$\hat{\theta}_k = \arcsin\left(\sqrt{\hat{u}_k^2 + \hat{v}_k^2}\right) = \arccos\left(\hat{w}_k\right) \tag{3-85}$$

$$\hat{\phi}_k = \arctan\left(\frac{\hat{v}_k}{\hat{u}_k}\right). \tag{3-86}$$

The polarization terms can be estimated by

$$\hat{\gamma}_k = \sum_{n=1}^{N} \arctan\left(\frac{\hat{g}_k 1}{\hat{g}_k 2}\right) \tag{3-87}$$

$$\hat{\eta}_k = \sum_{n=1}^{N} \angle \hat{g}_k 1\left(t_n\right) \tag{3-88}$$

where

$$\begin{aligned} \hat{\mathbf{g}}_k &= \begin{bmatrix} \hat{g}_{k1} \\ \hat{g}_{k2} \end{bmatrix} \\ &= \left[\mathbf{\Theta}_k^H\left(\hat{\theta}_k, \hat{\phi}_k\right)\mathbf{\Theta}_k\left(\hat{\theta}_k, \hat{\phi}_k\right)\right]^{-1}\mathbf{\Theta}_k^H\left(\hat{\theta}_k, \hat{\phi}_k\right)\hat{\mathbf{a}}_k. \end{aligned} \tag{3-89}$$

3.5.5 Verification of the ESPRIT algorithm implementation.

Verification of the ESPRIT algorithm was performed by Wong [15].

3.5.6 Constraints.

The number of signals for the ESPRIT algorithm must be assumed. The wavelength is needed to refine the estimate, but for the application in the HF band it is not used because the aperture is still small compared to wavelength. The ESPRIT algorithm used for this thesis capped the number of signals to 12. The cap is caused by the formation of the covariance matrices using two time-shifted sets of data.

3.6 The Experiment

The experiment is exploring both the utility of SQUIDs as a electrically small antenna element, and differentiation of co-channel signals using the SQUID elements. The simulation is divided into two different AoA estimation algorithms, and two different signal types. SPAWAR has expressed interest in co-channel SQUID behavior, and SPAWAR's interest has driven the choice of signals. The 3 signal simulation provides a single co-channel signal set and a single stand alone signal to provide a low saturation signal environment. The 6 signal environment provides 3 co-channel signal pairs for a medium saturation signal environment. The 12 and 15 signal environments are fully saturated environments. The tone signal type is used to simulate signals that are close to a normal transmitted signal. The gold code encoded signals are used to provide highly uncorrelated co-channel signals. The gold codes leverage the MUSIC algorithm's use of orthogonal spaces and a correlation matrix to differentiate signals.

The Gold code encoded signals are generated using initialization values [0 0 0 0 1] and [0 0 0 0 1] producing 33 fully orthogonal signals 31 bits long. The bits each represent a phase shift of π for each 1 and no shift for 0. The pattern generated by the 31 bit long sequence is repeated for the length of the signal. The orthogonality of the signals implies each signal does not correlate with other signals in the set. The gold codes were chosen as a backup in the event the tone signals correlated too

much with the co-channel signals. Correlation between signals can be a problem when simulating tone signals because the dynamics in the real world are difficult to fully simulate, and the algorithms use correlation matrices to generate the signal space and noise space. High correlation will cause the signals to be considered one, which causes the estimation to be a average of the two signals.

3.6.1 Statistical Analysis.

The series of experiments are run as single iterations, and not designed to provide statistical analysis. Statistical analysis was determined not to be necessary for the work's objectives due to the high signal to noise ratio of 43dB present when using 2D Bi-SQUIDs.

3.6.2 MUSIC Experiment.

The MUSIC array contains 16 identical 2D Bi-SQUID sensor elements arranged in a non-uniform planar array as depicted in Figure 13. The locations of the sensors is given in Table 2.

Table 2. SQUID Sensor Array Element Position in meters

$Sensor$	x_i	y_i	z_i
1	0	0	0
2	21.476	3.591	0
3	16.836	4.976	0
4	11.262	9.578	0
5	3.592	10.289	0
6	3.592	11.860	0
7	3.592	13.394	0
8	3.592	14.928	0
9	−3.592	14.928	0
10	−3.592	13.394	0
11	−3.592	11.860	0
12	−3.592	10.289	0
13	−11.262	9.578	0
14	−16.836	4.976	0
15	−21.476	3.591	0
16	6.024	−9.579	0

Table 3. Table of MUSIC Experiments

Total Number of Signals	Frequencies [MHz]	Number of Signals	Signal Type	Azimuth Range
3	3	2	Tone	−45 deg to 45 deg
	30	1		
6	3	2	Tone	−45 deg to 45 deg
	15	2		
	30	2		
15	3	2	Tone	−45 deg to 45 deg
	8	2		
	15	2		
	18	2		
	21	2		
	24	1		
	27	2		
	30	2		
3	3	2	Gold Code	−90 deg to 90 deg
	30	1		
6	3	2	Gold Code	−90 deg to 90 deg
	15	2		
	30	2		
15	3	2	Gold Code	−90 deg to 90 deg
	8	2		
	15	2		
	18	2		
	21	2		
	24	1		
	27	2		
	30	2		

3.6.3 ESPRIT Experiment.

The vector sensor ESPRIT array consists of 3 identical 2D Bi-SQUID sensor elements all of which are mutually orthogonal, and 3 ideal dipole antennas which are also mutually orthogonal. The ESPRIT algorithm uses 2 sets of 3 orthogonal magnetic field sensors that lie in a line with a parallel set of 3 orthogonal electric field sensors. The non-colocated AoA estimation uses sensor sets $(6, 7, 8)$ for the magnetic field components and $(10, 11, 12)$ for the electric field components as seen in Figure 17. The positions of the sensors shown in Figure 17 are shown in Table 4.

Table 4. Non-Colocated Vector SQUID Sensor Array Element Position in meters

Sensor	x_i	y_i	z_i
6	3.592	11.860	0
7	3.592	13.394	0
8	3.592	14.928	0
10	−3.592	13.394	0
11	−3.592	11.860	0
12	−3.592	10.289	0

There are six simulation environments run as described in Table 5. Each environment has the signals dispersed evenly across the azimuth range.

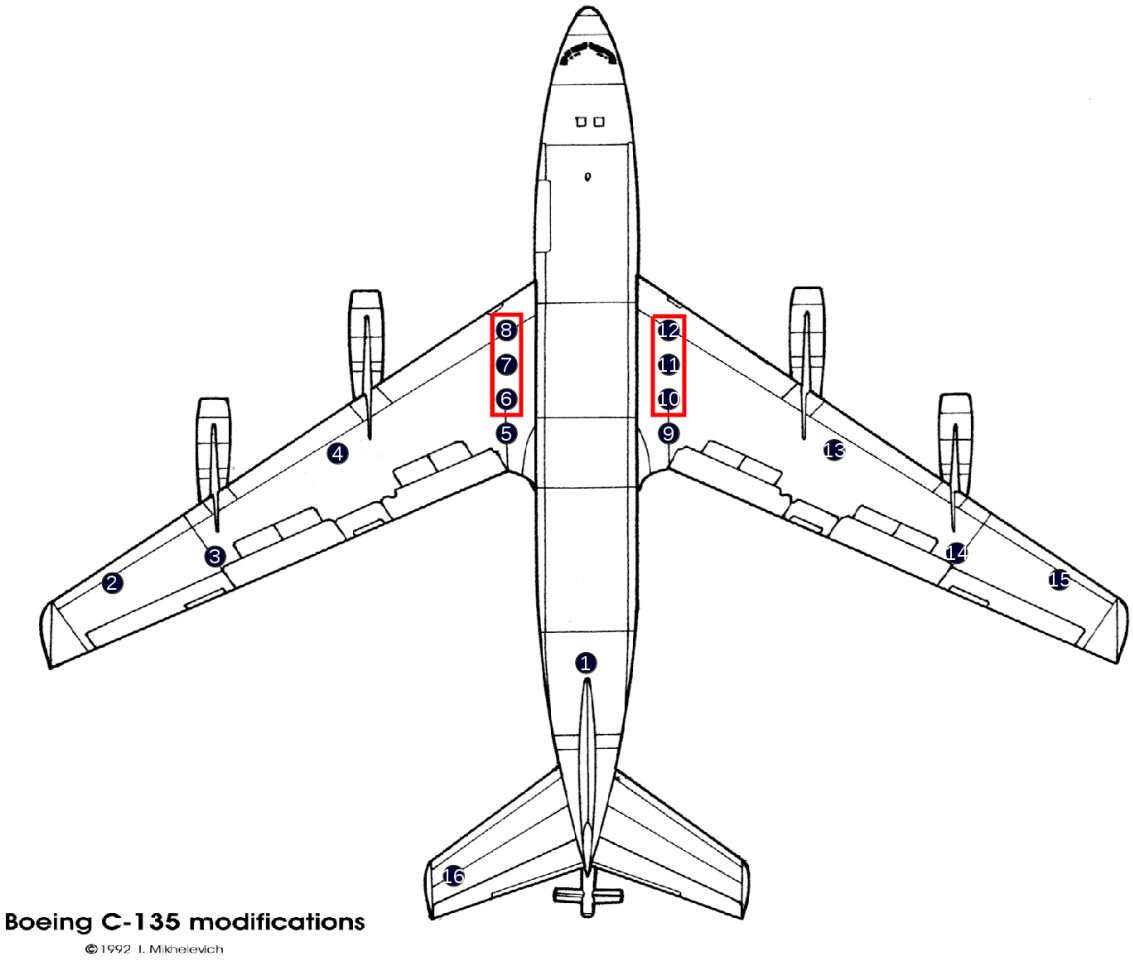

Figure 17. Non-Colocated Vector Sensor Placement on an RC-135. The boxes indicate the sensor positions used.

Table 5. Table of ESPRIT Experiments

Total Number of Signals	Frequencies [MHz]	Number of Signals	Signal Type	Azimuth Range
3	3	2	Tone	−45 deg to 45 deg
	30	1		
6	3	2	Tone	−45 deg to 45 deg
	15	2		
	30	2		
12	3	2	Tone	−90 deg to 90 deg
	15	2		
	18	1		
	21	2		
	24	1		
	27	2		
	30	2		
3	3	2	Gold Code	−90 deg to 90 deg
	30	1		
6	3	2	Gold Code	−90 deg to 90 deg
	15	2		
	30	2		
12	3	2	Gold Code	−90 deg to 90 deg
	15	2		
	18	1		
	21	2		
	24	1		
	27	2		
	30	2		

3.6.4 Code Components.

The simulation code is divided into a signal generator, a SQUID configuration file, a compiled SQUID simulation for the single element array, and 3 simulation compiled SQUID simulation for the vector sensor orthogonal sensor configuration. The signal generator creates a .mat file for each sensor position. The compiled code uses a spreadsheet file to control what files are loaded for each sensor simulation. This allows for the SPIRIT High Performance Computing (HPC) cluster to process each sensor simultaneously if resources are available. The flow of data is shown in Figures 18 and 19.

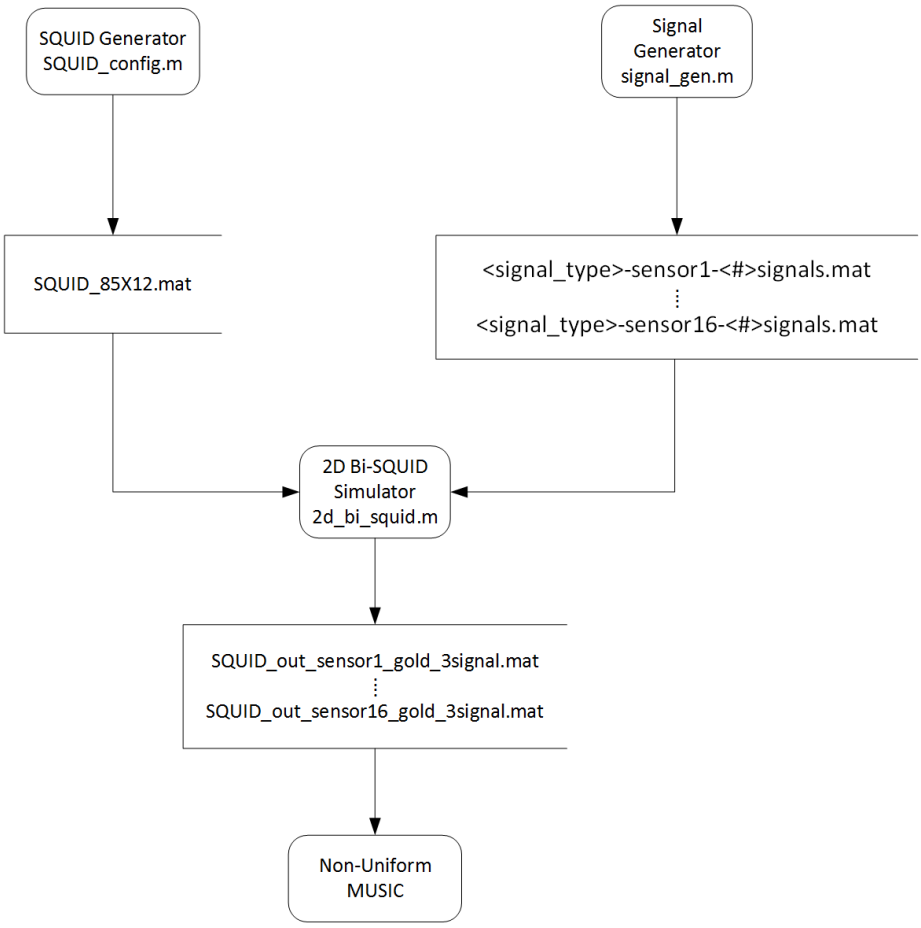

Figure 18. MUSIC Code Flow Chart

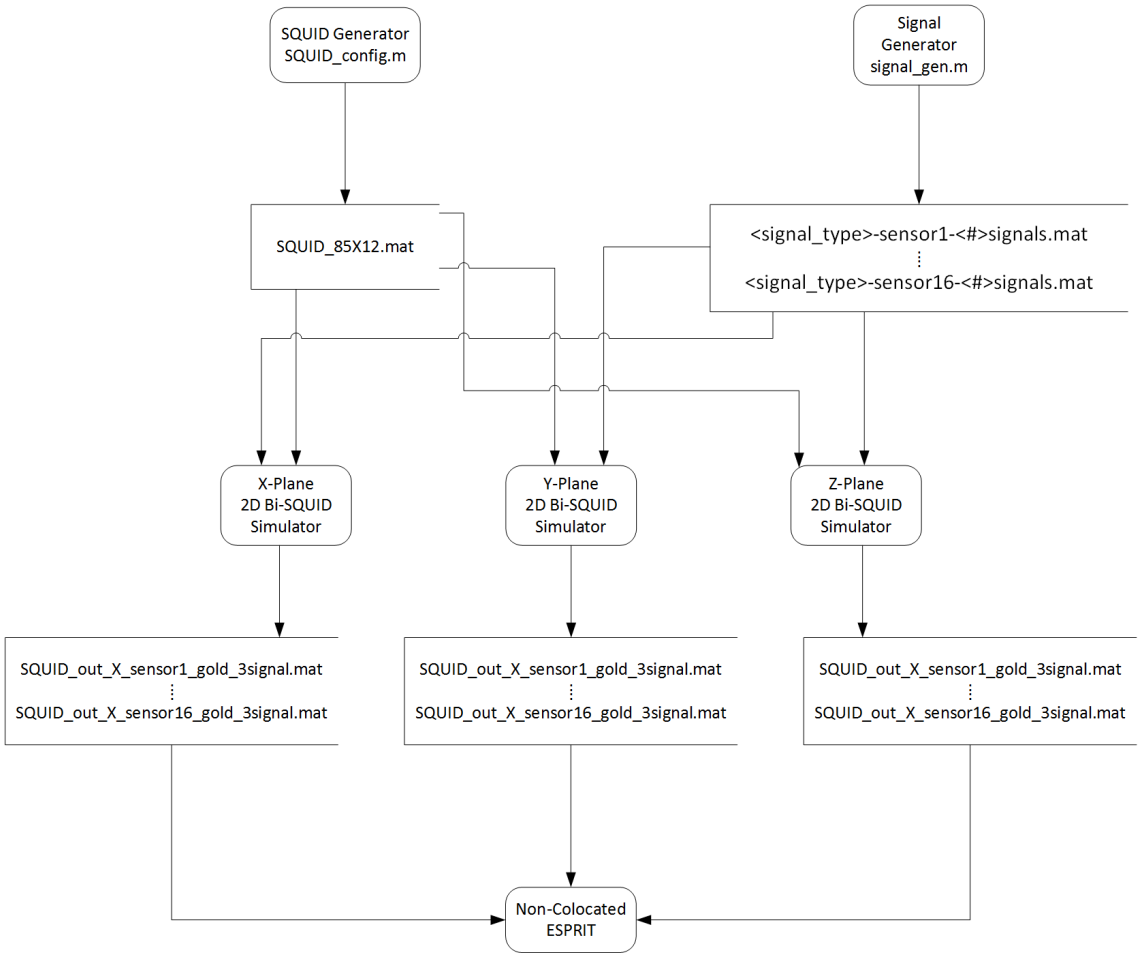

Figure 19. ESPRIT Code Flow Chart

3.7 Product

The product for each simulation sets consists of the MUSIC spectrum plot for the non-uniform array, compass plot for the non-colocated vector sensor ESPRIT estimated AoA, a compass plot showing the true AoA, and mean-squared-error for each scenario tested.

IV. Analysis

4.1 Introduction

Computer simulations of the Bi-Superconducting Quantum Interference Device (Bi-SQUID) arrays take about 50 minutes to complete on the SPIRIT High Performance Computing (HPC). Using the HPC allows each of the Bi-SQUID sensors to be simulated near simultaneously. The only thing preventing full simultaneous processing is that the HPC is a shared resource with other jobs in the queue and higher priority jobs taking precedence. The HPC allows the simulations to be completed much faster than on a local computer, which would run each task in a serial manner. The simulation run on the HPC SPIRIT cluster calculates the output of each Bi-SQUID sensor individually given a signal input in the form of the real components a vector of complex amplitudes. The sum of all incident signals is calculated by taking the sum of each signal incident on the sensor passed into the 2D Bi-SQUID model. The vector sensor implementation requires the signal to be projected to each of the X, Y, and Z orthogonal planes. In the following sections, the results of the simulations and Angle of Arrival (AoA) estimation is presented and a comparison is given with respect to which sensor element type is better suited for each High Frequency Direction Finding (HFDF) algorithm.

4.2 Non-uniform Array with Multi-Signal Classification (MUSIC)

In this section the performance of the 2D Bi-SQUID is compaired with the performance of a simulated electrically small dipole using the non-uniform MUSIC algorithm to estimate AoA. The expectation going into the MUSIC algorithm experiments is that the Bi-SQUID sensors will perform better due to the improved gain and reduced noise in the signal, but will be limited due to the physical constraints on the

array size which provides resolution to the MUSIC algorithm. In this discussion the angular error is the characteristic used to rate performance. The expectation going into this exploration is that the elevation angular resolution will be very coarse due to the elevation resolution being tied to the depth of the array and the spacing in wavelengths between each element. The azimuthal resolution should be better than the elevation, but still not optimal due to the spacing and overall size with respect to the wavelength of the signals under investigation.

4.2.1 Results.

The error of each simulation is displayed in Figures 20 thru 25. The 2D Bi-SQUID sensors tend to perform better than the typical antennas at low signal saturation, but as the signal space becomes more saturated, the typical antennas appear to perform better. The performance difference is expected due to the high gain of the Superconducting Quantum Interference Devices (SQUIDs) and low sensor noise.

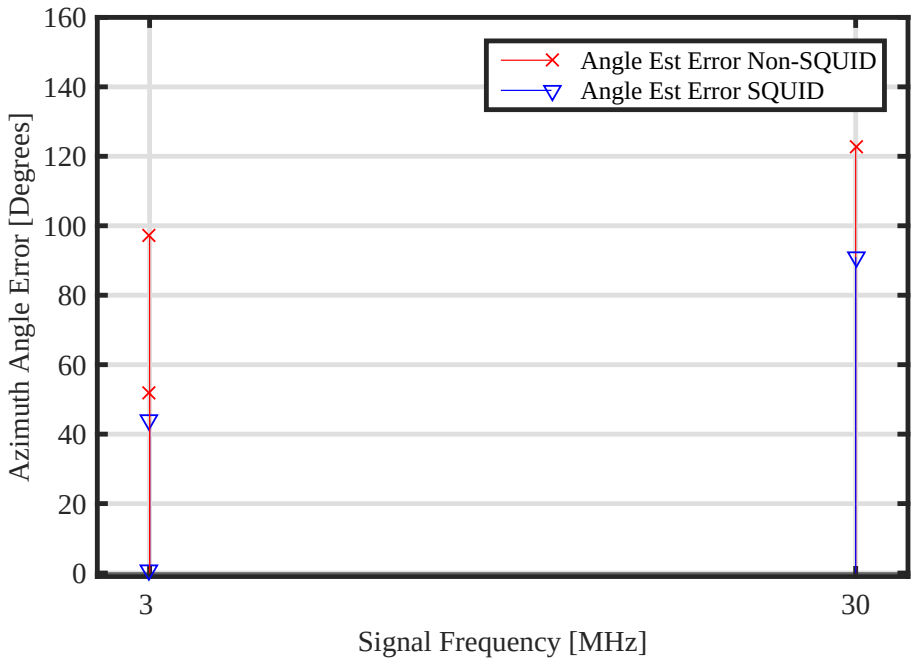

Figure 20. MUSIC Angular Error Plot for 3 Tone Signals

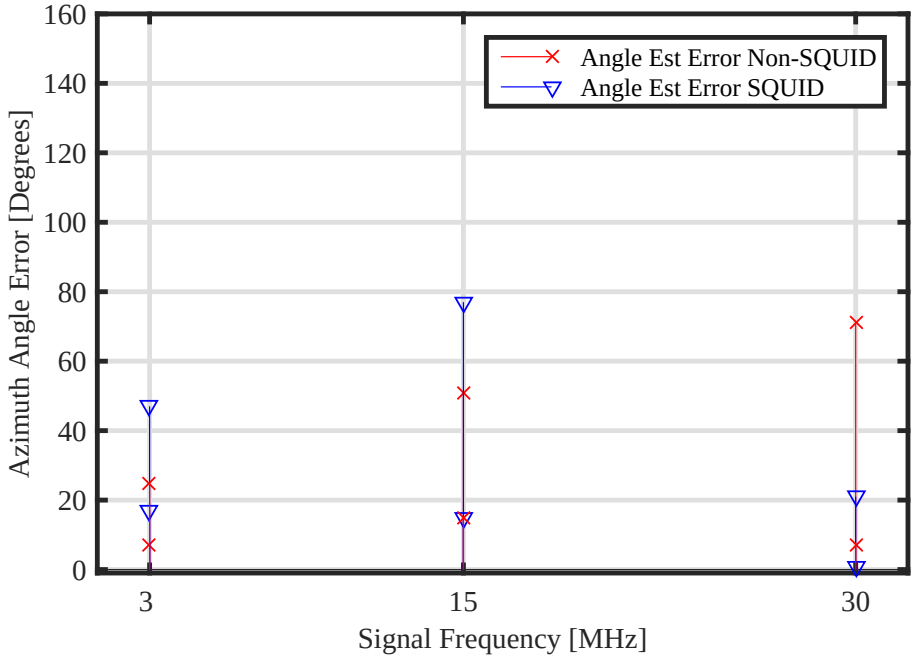

Figure 21. MUSIC Angular Error Plot for 6 Tone Signals

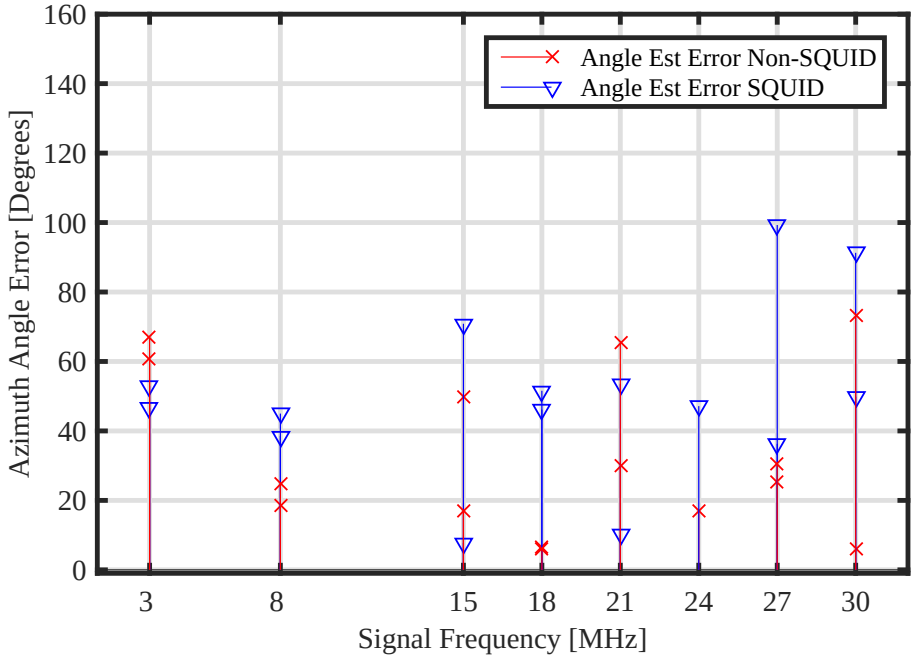

Figure 22. MUSIC Angular Error Plot for 15 Tone Signals

The 3 tone signal 2D Bi-SQUID MUSIC estimate is significantly better than the standard antenna. Surprisingly, the 30 MHz was not better than the 3 MHz signal set. The 6 tone signal set performed closer to what was expected for the 2D Bi-SQUIDs with respect to the 30 MHz performing better than the 3 MHz, but the 3 MHz and 15 MHz signals resolved better for the normal antenna than the 2D Bi-SQUID. The 15 tone signal scene shows some improvement and some worse. A statistical treatment of the normal signal would have been more telling because the signal to noise ratio is much lower then the 2D Bi-SQUID's.

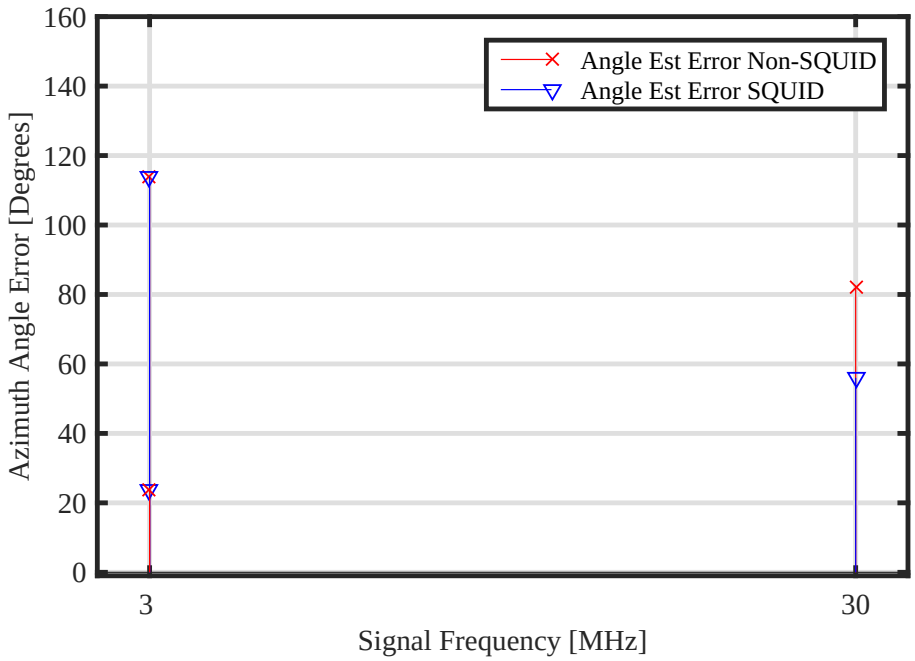

Figure 23. MUSIC Angular Error Plot for 3 Gold Code Signals

Use of Gold coded signals resulted in a larger discrepancy between Bi-SQUID and typical antenna performance with the Bi-SQUID outperforming the typical array. The single signal channel at 24 MHz showing no error for the 2D Bi-SQUID, and nearly 40 deg error on the normal antenna array is the most telling. All other bands have an assumption that the nearest of the 2 maximums is the peak associated with that signal, but with a single signal in the band there are no other signals that could

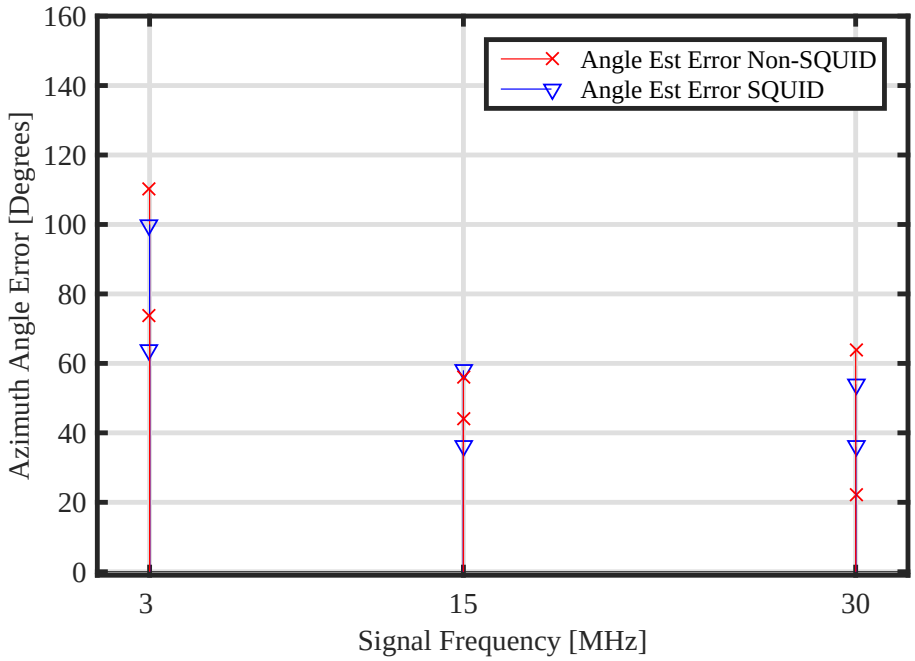

Figure 24. MUSIC Angular Error Plot for 6 Gold Code Signals

be confused in the algorithm.

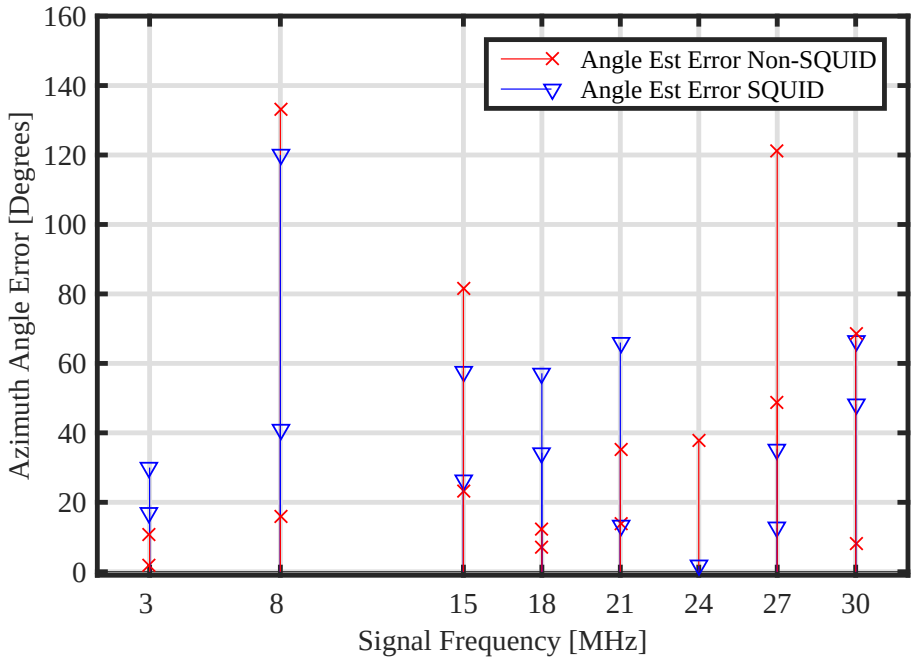

Figure 25. MUSIC Angular Error Plot for 15 Gold Code Signals

4.2.2 Analysis.

The MUSIC algorithm is based on correlation of signals and orthogonal noise and signal spaces. Signals are differentiated from one another based upon how well they correlate with one another. In reality, even tone signals transmitted using the same clock but at different locations and with different transmitters will not perfectly correlate. There is noise added to the transmitted signal from the transmitter along with path effects related to the atmosphere and reflections. The signal generation model was designed to create the signals in a way to prevent the signals from appearing as perfect tones without any aspect related distortions. Since real world signals do not correlate well unless they are transmitted from the same location using the same transmitting media, it is expected that the non-uniform MUSIC method is able to determine an AoA estimate of signals sharing the same frequency as well as those that do not. Though it should be noted that as the wavelength grows long to the array size the MUSIC algorithm has difficulty differentiating the signals apart. The

difficulty in differentiation is evident when considered in terms of Fourier frequency space. The larger the array with respect to wavelength, the finer the ability to resolve the location of a transmitted beam. The resolution effect is related to the effect seen whan a beam is transmitted from an electrically large array it is narrower and more directable than one in an electrically small array. Beyond the physical constraints, the 2D Bi-SQUIDs provide a slight improvement from the standard sensor, and suggest the possibility if better tuned and an experiment run where the array was interrogated at all angles by a single signal and compared to a statistically significant analysis of the normal antenna array performed that the results would be significantly better. Additionally a prime number of MHz frequency sequence would have reduced the harmonic induced error.

4.3 Non-Colocated Vector Sensors with ESPRIT

In this section the performance of 2D Bi-SQUIDs as magnetic field sensors in the non-colocated Estimation of Signal Parameters via Rotational Invariance Techniques (ESPRIT) algorithm is reviewed along with a discussion reviewing why the non-colocated ESPRIT algorithm performed the way it did compared to a normal non-colocated vector sensor. In this discussion the angular error is the characteristic used to rate performance. The expectation is that the algorithm should perform better using the SQUID sensors due to the higher gain and lower noise. The non-colocated approach reduces cross coupling of the antenna elements due to spacial separation, but for a colocated normal vector sensor, cross coupling would also be improved using the SQUID sensors. Cross coupling is neglected, for this experiment, beyond the internal dynamics of the 2D Bi-SQUID sensor. Additionally, the non-colocated implementation of the vector sensor is expected to provide reduced error as the aperture increases in size with respect to wavelength.

4.3.1 Results.

The error of each simulation is displayed in Figures 26 to 30. The 2D Bi-SQUID sensors tend to perform better than the typical antennas at low signal saturation, but as the signal space becomes more saturated, the typical antennas appear to perform better. The performance difference is expected due to the high gain of the SQUIDs and low sensor noise. Additionally, the 3 MHz channel does better than the 30 MHz band as expected given vector sensor is designed to perform best when electrically small, and the portions of the non-colocated algorithm that can leverage increase aperture is not optimized given the short set of parallel sensors available in the chosen footprint. In Figure 27 the 2d Bi-SQUID outperforms the normal sensor in each channel, and in Figures 28 through 30 the 2d Bi-SQUID outperforms the normal sensor in the majority of the channels.

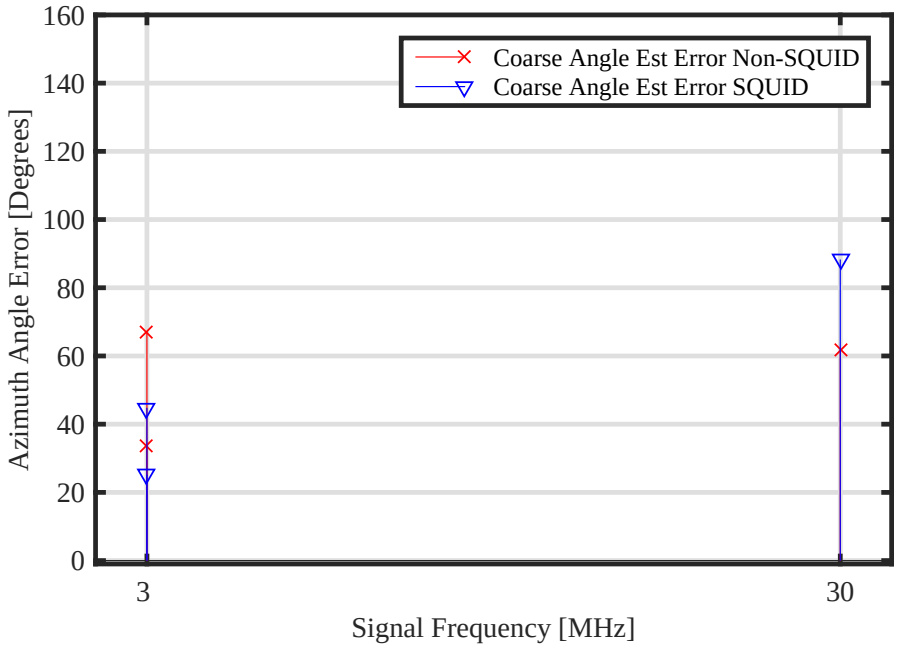

Figure 26. ESPRIT Angular Error Plot for 3 Gold Code Signals

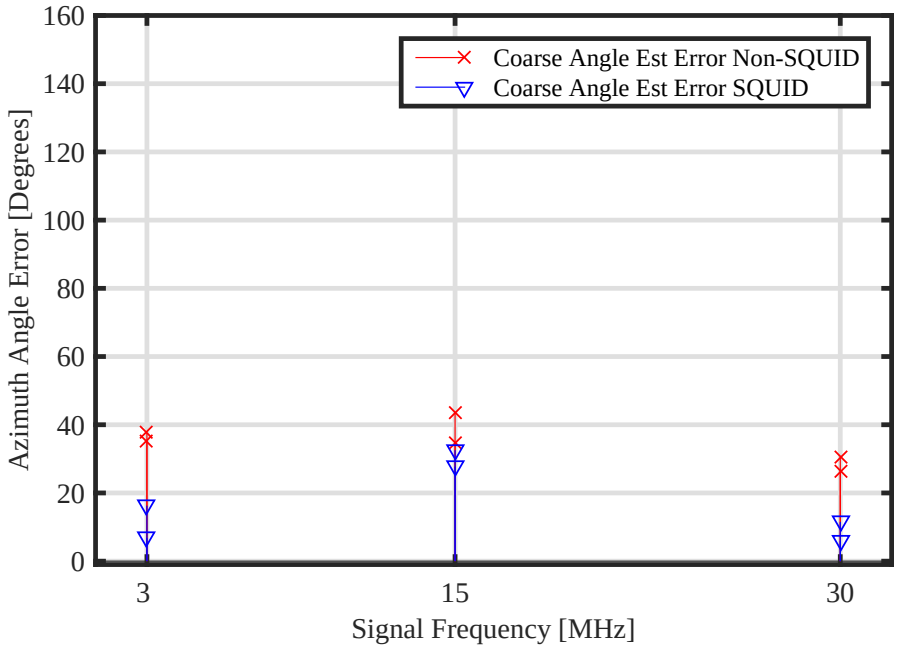

Figure 27. ESPRIT Angular Error Plot for 6 Gold Code Signals

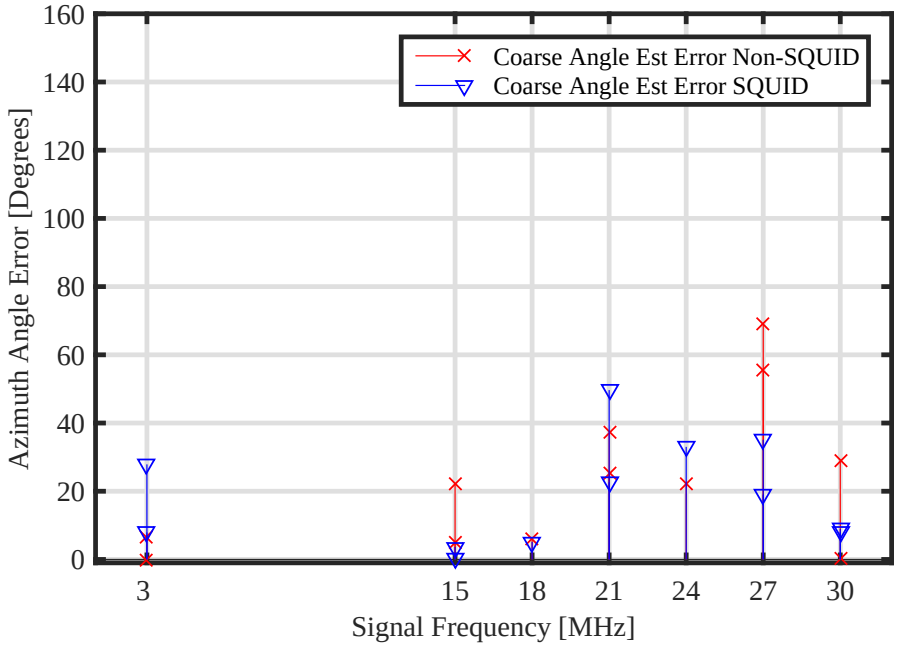

Figure 28. ESPRIT Angular Error Plot for 12 Gold Code Signals

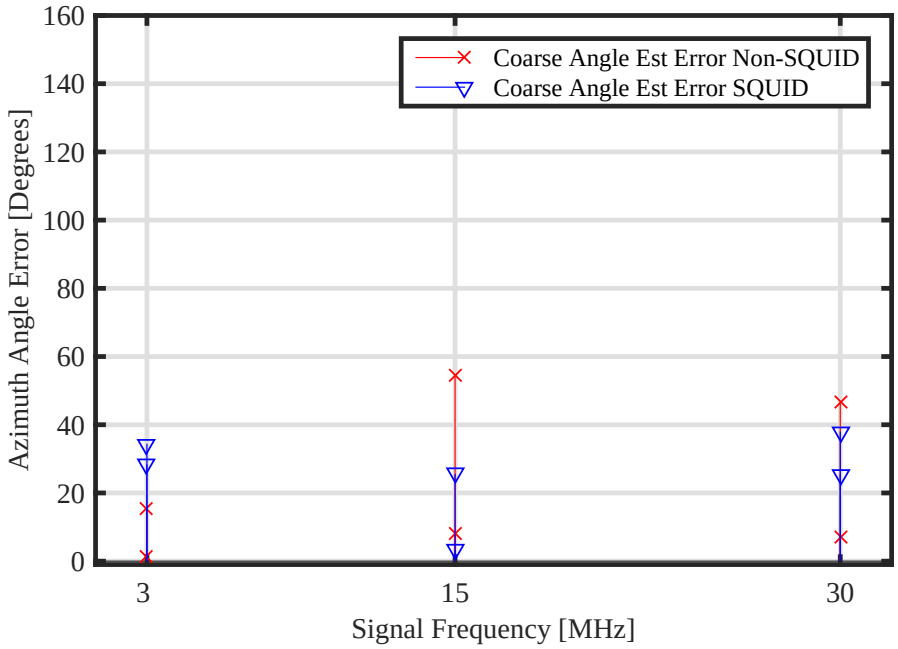

Figure 29. ESPRIT Angular Error Plot for 6 Tone Signals

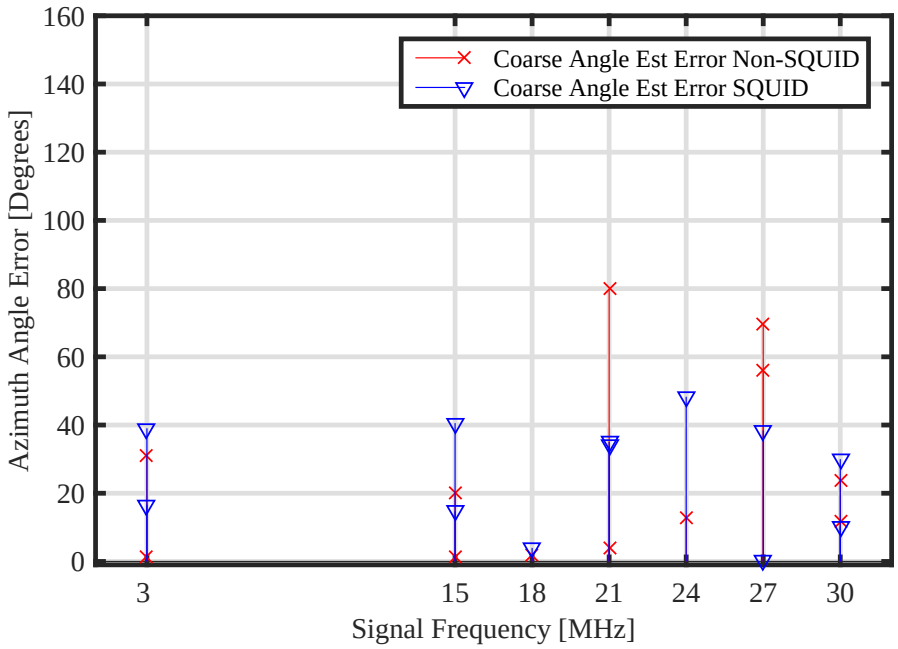

Figure 30. ESPRIT Angular Error Plot for 12 Tone Signals

4.3.2 Analysis.

The performance of the non-colocated ESPRIT algorithm is expected to perform well under electrically small conditions. Vector sensors are designed to be comprised of electrically small dipoles to detect the electric field and small loop antennas for the magnetic field. The 2D Bi-SQUID sensors are much more sensitive than a normal loop antenna. The increased sensitivity implies that the 2D Bi-SQUID sensors should out perform a normal loop as long as the sensor does not saturate causing loss of signal information. The ESPRIT algorithm does not have any difficulty differentiating cochannel signals.

The non-colocated vector sensor attempts to take advantage of an increased aperture to improve the resolution of the estimated $\hat{u}$ and $\hat{v}$. The expected improvement is minimal until the distance between the x and y component sensors is greater than λ. For the simulations run during this thesis, none of the spacing is greater than λ, so there is not an expected gain. Increasing the span of the array along the fuselage of the RC-135 is a suggested topic for future study.

The algorithm as implemented produced an abnormality that caused the signals to always be placed in the first angular quadrant. The abnormality appears to be caused by the algorithms assumption that the signals exist from 0 deg to 180 deg. The signals simulated in this effort were generated between -90 deg and 90 deg which appears to have cause the ambiguity in angular resolution. Additionally, the algorithm is designed to estimate the parameters of the unit vector weights to resolve the AoA which results in low apparent error and Cramer-Rao Lower Bound (CRLB) [15], but can result in very large angular error as seen in Figure 31 compared to 26.

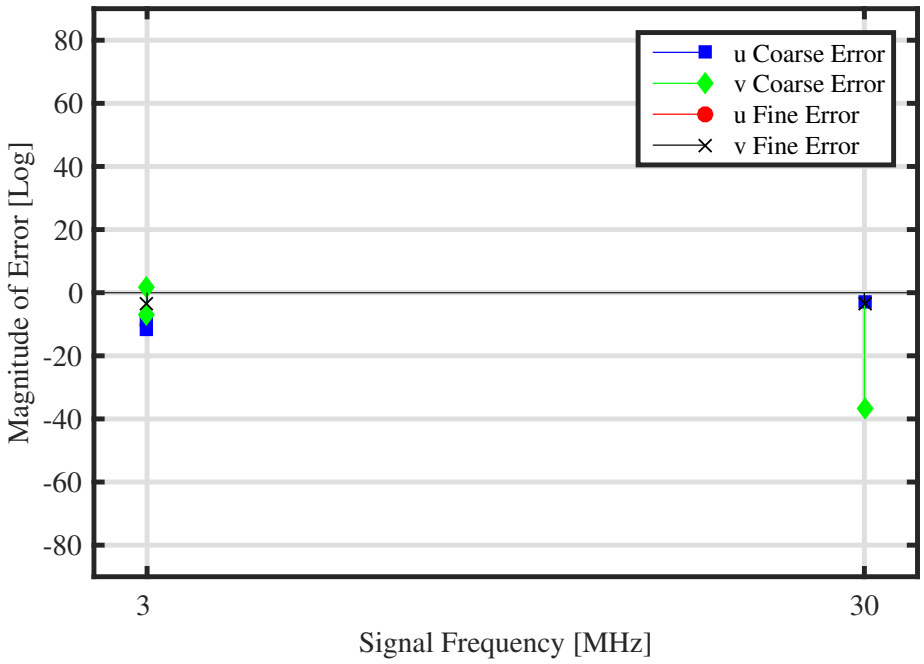

Figure 31. This figure shows the error for the estimated magnitude of the orthogonal unit vecors $\hat{v}$ and $\hat{u}$ for 3 gold code encoded signals

4.4 Comparison

Though the improvement is not awe inspiring, the 2D Bi-SQUID does demonstrate improved performance. With optimized positioning of sensors, tuned 2D Bi-SQUID model, and an experiment designed to purely determine AoA performance, the 2D Bi-SQUID sensor appears to be a good option. The MGL-S8A B-dot sensor for > 76 MHz is 0.1 square meters[3], and there doesn't appear to be one at the > 3 MHz size. The 2D Bi-SQUID sensor can be as small as 0.01 square meters. Video playback of the simulated 2D Bi-SQUID did not display any noticeable phase distortion until leaving the linear region.

V. Conclusion

5.1 Summary

This thesis has presented a brief history of Superconducting Quantum Interference Devices (SQUIDs) and Direction Finding (DF) techniques, followed by a presentation of the derivation of the two chosen Angle of Arrival (AoA) estimation techniques used to assess the initial feasibility of SQUID sensors for co-channel signal discrimination and High Frequency Direction Finding (HFDF) sensors. The 2D Bi-Superconducting Quantum Interference Device (Bi-SQUID) sensors provided some noticeable improvement in two DF algorithms over typical antenna elements in some cases. The performance is less then expected given the large increase in signal gain for an electrically small sensor and significant reduction in noise. The AoA estimation did not give any indication that SQUIDs perform any better then traditional antennas but the gain and noise characteristics suggest that there is potential further improvement.

The algorithms used to perform the AoA estimation need to be improved upon and new algorithms explored. The 2D Bi-SQUID configuration needs to be fine-tuned to the target band and signal strength. The SQUID based sensors demonstrated the ability to be used in co-channel signal differentiation and AoA estimation.

5.2 Lessons Learned

The first lesson learned is that there is a need to fully characterize the sensor model prior to starting any testing. Fine tuning the SQUID to the task includes determining the best number of SQUIDs in series and in parallel. The target signal level should be the center of the linear region of the linear range plot. The linear range should be plotted for each frequency used in order to ensure that the bias is selected to place the signal power close to center for all frequencies considered. Clipping occurs when

there is not enough linear range or if the bias is off center, causing either the top or the bottom to clip. Clipping could be a possible cause for the effects seen in the signal saturated sceen.

The non-colocated Estimation of Signal Parameters via Rotational Invariance Techniques (ESPRIT) algorithm should be simulated using transmit angles bounded by 0 deg to 180 deg. The angular range is the cause for all the angle estimations being in the first quadrant.

A statistical analysis must be accomplished using a minimum of 1000 using root-mean-square errors to compare errors. For this Monte Carlo analysis, 2 signals should be transmitted from 2 constant locations. Keeping it consistent would reduce the data size and book-keeping requirements, while improving High Performance Computing (HPC) ease of use and still providing statistically significant results.

Testing signal saturation should be conducted using non-harmonic signals. For example, the High Frequency (HF) band should use the prime number frequencies- 3 MHz, 5 MHz, 7 MHz, 11 MHz, 13 MHz, 17 MHz, 19 MHz, 23 MHz, 27 MHz, and 29 MHz. Additionally, 4 MHz or one of its harmonics can be added as well if necessary.

5.3 Future Work

Further exploration in the area of the non-colocated vector sensor approach and optimizing the placement of elements will provide a better assessment of the algorithm's utility for HFDF. In addition, exploring the use of superconducting dipole elements as well may provide added improvements as seen in [9], where Mazlina Esa studied the use of high critical temperature superconductors like yttrium-barium-copper-oxide (YBCO) as meander dipole antennas. Another area to explore would be the Tri-SQUID configuration suggested by Shane Cybart in [10], where he uses a 2D Direct Current Superconducting Quantum Interference Device (DC-SQUID) ar-

ray with SQUID loop area sized in a Fourier series pattern to produce a very simple model to reduce the computational complexity of simulation the SQUID system. The sparse triangular array purposed [23] where a loop triad is used with a dipole triad and a single dipole may also provide improved performance. SQUIDs are immensely sensitive devices that reliably detect signals, the remaining challenge is our processing capability in order to full utilize SQUID technology.

Bibliography

1. Susan Anne Elizabeth Berggren, *Computational and mathematical modeling of coupled superconducting quantum interference devices*, Ph.D. thesis, Claremont Graduate School, 2012.

2. V. K. Kornev, I. I. Soloviev, N. V. Klenov, and O. A. Mukhanov, "Bi-SQUID: a novel linearization method for dc SQUID voltage response," *Superconductor Science and Technology*, vol. 22, no. 11, pp. 114011, 2009.

3. Michael D Archer, "High Frequency Magnetic Field Direction Finding Using MGL-S8A B-dot Sensors," M.S. thesis.

4. Clair F. Corbin, "High Frequency Direction Finding Using Structurally Integrated Antennas on a Large Airborne Platform," M.S. thesis.

5. Travis Abeita, "Superconducting quantum interference devices for the detection of magnetic flux and application to airborne high frequency direction finding," M.S. thesis, Air Force Institute of Technology, 2015.

6. V. K. Kornev, I. I. Soloviev, N. V. Klenov, and O. A. Mukhanov, "Progress in high-linearity multi-element josephson structures," *Physica C: Superconductivity*, vol. 470, no. 19, pp. 886–889, 2010.

7. Dirk Van Delft and Peter Kes, "The discovery of superconductivity The discovery of superconductivity feature," vol. 63, no. 9, pp. 38–42, 2010.

8. John Clarke and Alex I. Braginski, *The SQUID Handbook: Vol 1 Fundamental and Technology of SQUIDs and SQUIDs Systems*.

9. Mazlina Esa, *Electrically Small High-Temperature Superconducting Y-Ba-Cu-O Meander Dipole Antennas for Space-Limited Applications*, Ph.D. thesis, 1996.

10. Shane A Cybart, EY Cho, TJ Wong, VN Glyantsev, JU Huh, CS Yung, BH Moeckly, JW Beeman, E Ulin-Avila, SM Wu, and RC Dynes, "Large voltage modulation in magnetic field sensors from two-dimensional arrays of y-ba-cu-o nano josephson junctions," *Applied Physics Letters*, vol. 104, no. 6, pp. 062601, 2014.

11. Susan Berggren, Georgy V Prokopenko, P Longhini, A Palacios, Oleg Mukhanov, Anna Leese de Escobar, BJ Taylor, MC De Andrade, M Nisenoff, Robert L Fagaly, et al., "Development of 2-d bi-squid arrays with high linearity," *Applied Superconductivity, IEEE Transactions on*, vol. 23, no. 3, pp. 1400208–1400208, 2013.

12. Patrick Longhini, Susan Berggren, Anna Leese de Escobar, Antonio Palacios, Sarah Rice, Benjamin Taylor, Visarath In, Oleg A Mukhanov, Georgy Prokopenko, Martin Nisenoff, et al., "Voltage response of non-uniform arrays of bi-superconductive quantum interference devices," *Journal of Applied Physics*, vol. 111, no. 9, pp. 093920, 2012.

13. Shane a. Cybart, E. Y. Cho, T. J. Wong, V. N. Glyantsev, J. U. Huh, C. S. Yung, B. H. Moeckly, J. W. Beeman, E. Ulin-Avila, S. M. Wu, and R. C. Dynes, "Large voltage modulation in magnetic field sensors from two-dimensional arrays of Y-Ba-Cu-O nano Josephson junctions," *Applied Physics Letters*, vol. 104, no. 6, pp. 062601, 2014.

14. II Soloviev, VK Kornev, NV Klenov, and OA Mukhanov, "Superconducting josephson structures with high linearity of transformation of magnetic signal into voltage," *Physics of the Solid State*, vol. 52, no. 11, pp. 2252–2258, 2010.

15. Kainam Thomas Wong and Xin Yuan, "vector cross-product direction-finding with an electromagnetic vector-sensor of six orthogonally oriented but spatially noncollocating dipoles/loops," *Signal Processing, IEEE Transactions on*, vol. 59, no. 1, pp. 160–171, 2011.

16. P. Yan M. Brewer T. Van, J. Berrie and D. Latypov, *Direction finding approaches for high frequency applications*, BerrieHill Research Corperation, Tech. Rep., 2009.

17. Mark A Richards, Jim Scheer, William A Holm, et al., *Principles of modern radar: basic principles*, SciTech Pub., 2010.

18. T Engin Tuncer and Benjamin Friedlander, *Classical and modern direction-of-arrival estimation*, Academic Press, 2009.

19. Kainam Thomas Wong, "Direction finding/polarization estimationdipole and/or," *Aerospace and Electronic Systems, IEEE Transactions on*, vol. 37, no. 2, pp. 679, 2001.

20. Carl Theodore Adolf Johnk, *Engineering electromagnetic fields and waves*, vol. 1, 1975.

21. Arye Nehorai and Eytan Paldi, "Vector-sensor array processing for electromagnetic source localization," *Signal Processing, IEEE Transactions on*, vol. 42, no. 2, pp. 376–398, 1994.

22. Kainam T Wong and Michael D Zoltowski, "Uni-vector-sensor esprit for multisource azimuth, elevation, and polarization estimation," *Antennas and Propagation, IEEE Transactions on*, vol. 45, no. 10, pp. 1467–1474, 1997.

23. Feng Luo and Xin Yuan, "Enhanced" vector-cross-product" direction-finding using a constrained sparse triangular-array," *EURASIP Journal on Advances in Signal Processing*, vol. 2012, no. 1, pp. 1–11, 2012.

AFIT Air Force Institute of Technology

AFRL Air Force Research Laboratory

AoA Angle of Arrival

BRC BerrieHill Research Corporation

Bi-SQUID Bi-Superconducting Quantum Interference Device

CRLB Cramer-Rao Lower Bound

DC-SQUID Direct Current Superconducting Quantum Interference Device

DF Direction Finding

EM electromagnetic

ESPRIT Estimation of Signal Parameters via Rotational Invariance Techniques

HF High Frequency

HFDF High Frequency Direction Finding

HPC High Performance Computing

HPCMP High Performance Computing Modernization Program

ISR Intelligence, Surveillance and Reconnaissance

MLE Maximum Likelihood Estimator

MUSIC Multi-Signal Classification

PEC Perfect Electrical Conductor

PMC Perfect Magnetic Conductor

R-SQUID Resister Superconducting Quantum Interference Device

RF Radio Frequency

RF-SQUID Radio Frequency Superconducting Quantum Interference Device

SIGINT Signals Intelligence

SNR Signal to Noise Ratio

SPAWAR Space and Naval Warfare Systems Command

SQIF Superconducting Quantum Interference Filter

SQUID Superconducting Quantum Interference Device

Tri-SQUID Triangular wave SQUID

TEM Transvers Electromagnetic

YBCO yttrium-barium-copper-oxide

REPORT DOCUMENTATION PAGE

Form Approved
OMB No. 0704–0188

1. REPORT DATE *(DD–MM–YYYY)*	2. REPORT TYPE	3. DATES COVERED *(From — To)*
24–03–2016	Master's Thesis	Sept 2014 — March 2016

4. TITLE AND SUBTITLE

Superconducting Quantum Interference Device Array Based High Frequency Direction Finding on an Airborne Platform

5a. CONTRACT NUMBER

5b. GRANT NUMBER

5c. PROGRAM ELEMENT NUMBER

6. AUTHOR(S)

Kvasager, Tyrel K, Capt

5d. PROJECT NUMBER

15G186

5e. TASK NUMBER

5f. WORK UNIT NUMBER

7. PERFORMING ORGANIZATION NAME(S) AND ADDRESS(ES)

Air Force Institute of Technology
Graduate School of Engineering and Management(AFIT/EN)
2950 Hobson Way
WPAFB OH 45433-7765

8. PERFORMING ORGANIZATION REPORT NUMBER

AFIT-ENG-MS-16-M-028

9. SPONSORING / MONITORING AGENCY NAME(S) AND ADDRESS(ES)

Air Force Research Laboratory, Multispectral Sensing & Detection Division, RF Systems Branch
Attn: Charles Cerny
2241 Avionic Circle
Area B, B620
San Diego, CA 92110
(312)798-8248 charles.cerny.1@us.af.mil

10. SPONSOR/MONITOR'S ACRONYM(S)

AFRL/RYMR

11. SPONSOR/MONITOR'S REPORT NUMBER(S)

12. DISTRIBUTION / AVAILABILITY STATEMENT

DISTRIBUTION STATEMENT A:
APPROVED FOR PUBLIC RELEASE; DISTRIBUTION UNLIMITED.

13. SUPPLEMENTARY NOTES

14. ABSTRACT

This thesis evaluates a new incredibly sensitive highly linear high dynamic range 2D Bi-SQUID array purposed by the dissertation written by Susan Berggren [1] applied to use on an airborne platform for the purposes of HFDF. To evaluate how useful the 2D Bi-SQUID is we explore multiple signals of the same frequency in two different base sensor configurations: Non-uniform phased array and non-colocated Poynting's Theorem based vector sensors. The exploration is performed using the SPIRIT HPC system to calculate the 2D Bi-SQUID output given multiple incident signals. The AoA estimation calculation is performed using the MUSIC algorithm on the signals received on the non-uniform phased array, and the ESPRIT algorithm is used on the signals received on the non-colocated vector sensor. The simulation results show that the MUSIC algorithm using 2D Bi-SQUIDs is able to differentiate two signals that are of the same frequency, but the resolution and accuracy of the algorithm is poor due to the size of the phased array on the airborne platform. The non-colocated ESPRIT using 2D Bi-SQUIDs performs, but still has less than desirable angular error.

15. SUBJECT TERMS

SQUID, High Frequency Direction Finding, Vector Sensor, Phased Array, HPCMP, MUSIC, ESPRIT, Non-Colocated, Non-Uniform, Electrically Small, SQUIF, Bi-SQUID, 2D Bi-SQUID, Superconducting Quantum Interference Device

16. SECURITY CLASSIFICATION OF:			17. LIMITATION OF ABSTRACT	18. NUMBER OF PAGES	19a. NAME OF RESPONSIBLE PERSON
a. REPORT	b. ABSTRACT	c. THIS PAGE			Lt. Col. J. Stringer, AFIT/ENG
U	U	U	U	92	19b. TELEPHONE NUMBER *(include area code)* (937) 255-3636, x4555; jeremy.stringer@afit.edu